THE ASTROPHYSICAL JOURNAL, 405:249–267, 1993 March 1

CO LINES TOWARD NGC 2024 AND OTHER STAR-FORMING REGIONS: A CLOSER LOOK AT THE WARM GAS COMPONENT

U. U. GRAF,[1] A. ECKART, R. GENZEL, A. I. HARRIS, A. POGLITSCH, A. P. G. RUSSELL,[2] AND J. STUTZKI[3]
Max-Planck-Institut für extraterrestrische Physik, D-8046 Garching, bei München, Germany
Received 1992 April 9; accepted 1992 September 8

ABSTRACT

We present observations of ^{13}CO $J = 6 \rightarrow 5$ emission from a variety of Galactic star-forming regions. Sources spanning a luminosity range from 1 to 10^6 $L_\odot$ have been detected in this isotopic transition. The high line intensity (typically $T_{mb} = 20$–100 K) confirms the presence of large column densities ($N_{H_2} \approx 10^{23}$ cm^{-2}) of warm ($T_{kin} \geq 100$ K) molecular gas in typical regions of massive star formation. The $^{13}CO/^{12}CO$ $J = 6 \rightarrow 5$ intensity ratio is typically much higher than the $^{13}CO/^{12}CO$ abundance ratio. Hence, even the mid-J transitions of the main CO isotope are very optically thick in most sources.

The ^{13}CO $6 \rightarrow 5$ emission is found to arise from quiescent ($\Delta v \approx 5$ km s^{-1}) gas. Strip maps of selected sources (M17, Cepheus A, W51) show that the ^{13}CO $6 \rightarrow 5$ emitting gas is confined to narrow zones (<1 pc) close to the H II regions in these star-forming regions. Thus, the spatial distribution and the quiescence of the warm gas support the idea that it is being heated by the UV radiation field just outside the H II regions. Although the column density of the warm gas is much higher than predicted by present photodissociation region (PDR) models, photoheating seems to be the most probable dominating heating process in these regions.

We further present a detailed multiline study of the molecular gas in a selected source: NGC 2024. Measurements of nine different CO lines enable us to derive precise physical parameters of the two major source components along the line of sight toward the mm continuum peak FIR 5. The component in front of the H II region is cold ($\approx$23 K) and contains about one-fifth of the total molecular column density (5×10^{22} cm^{-2}). The bulk of the column density (2×10^{23} cm^{-2}) is located behind the H II region in a warm (67 K) gas component. For a standard H_2/CO ratio, the low intensity of low-J isotopic CO lines excludes the presence of large amounts ($N_{H_2} \geq 10^{24}$ cm^{-2}) of cold ($T_{kin} < 25$ K) molecular gas. Maps recorded in four CO transitions indicate that the warm gas is located in the immediate vicinity of the H II region and that its spatial distribution is very similar to the 1.3 mm dust continuum. The 1.3 mm continuum, therefore, is likely to originate from—probably warm— dust embedded within warm gas.

Subject headings: ISM: individual (NGC 2024, M17, S106, W51) — radio lines: ISM — stars: formation

1. INTRODUCTION

During the past few years submillimeter and far-infrared observations of carbon monoxide (CO) yielded substantial evidence for the presence of large amounts of warm molecular gas in regions of massive star formation (Jaffe, Harris, & Genzel 1987; Harris et al. 1987b; Genzel, Poglitsch, & Stacey 1988; Schmid-Burgk et al. 1989; Boreiko, Betz, & Zmuidzinas 1989). The recent measurements of isotopic ^{13}CO $J = 6 \rightarrow 5$ in Orion and NGC 2024 (Graf et al. 1990, hereafter Paper I) provided more accurate column density values for the warm gas component. In the Orion Bar and in NGC 2024 the column densities of warm molecular hydrogen ($T_{kin} \geq 100$ K) are found to be $\approx 10^{23}$ cm^{-2}, up to one-third of the gas mass. In order to determine whether these high column densities of warm gas are typical for regions of massive star formation, we studied the ^{13}CO $J = 6 \rightarrow 5$ emission from a large sample of luminous star-forming regions.

In addition to the survey of the submillimeter CO line properties of star formation regions, we performed a detailed multiline study of NGC 2024, an example of a nearby (415 pc; Anthony-Twarog 1982) massive star-forming region. The many lines with different excitation conditions we measured in this source enable us to establish the source structure and the relationship between the warm molecular gas component and the colder cloud material. We will also be able to explain the apparent velocity shift between ^{13}CO and ^{12}CO mid-J lines, which we noted earlier (Paper I).

The comparison of millimeter and submillimeter main- and rare-isotopic line shapes illustrated the necessity of observing many transitions of rare isotopes, not only in order to constrain the optical depth of the line, but also to detect self-absorption effects and to separate individual source components along the line of sight.

2. OBSERVATIONS

Table 1 lists the CO observations carried out in the various sources. Source positions are listed in Table 2. The $J = 7 \rightarrow 6$ and $6 \rightarrow 5$ lines have been observed with the MPE cooled Schottky submillimeter heterodyne receiver (Harris et al. 1987a) at the James Clerk Maxwell Telescope (JCMT) and the United Kingdom Infrared Telescope (UKIRT) on Mauna Kea/Hawaii. The data were calibrated in the way described by Harris (1986), Harris et al. (1987b), Paper I, and Graf (1991). The estimated calibration uncertainty is about 30%.

[1] Postal address: Department of Astronomy, R. L. Moore Hall 15:308, University of Texas at Austin, Austin, TX 78712.
[2] Postal address: Royal Observatory Edinburgh, Blackford Hill, Edinburgh, EH9 3HJ, Scotland.
[3] Postal address: Physikalisches Institut, Universität zu Köln, Zülpicher Straße 77, D-5000 Köln 41, Germany.

TABLE 1

MULTILINE CO OBSERVATIONS IN STAR-FORMING REGIONS

Transition	ν (GHz)	Telescope	Beam	Date	Map Size
		NGC 2024			
CO $J = 7 \rightarrow 6$	806.652	UKIRT	25″	1989 Jan 23	105″ × 165″
CO $J = 6 \rightarrow 5$	691.473	JCMT	8	1989 Dec	...
^{13}CO $J = 6 \rightarrow 5$[a]	661.067	JCMT	8	1989 Nov	...
CO $J = 3 \rightarrow 2$	345.796	IRAM 30 m	8	1990 Feb 16	...
^{13}CO $J = 3 \rightarrow 2$	330.588	IRAM 30 m	8	1990 Feb 11	67″ × 135″
^{13}CO $J = 3 \rightarrow 2$	330.588	JCMT	15	1989 Dec	25 spectra
C^{17}O $J = 2 \rightarrow 1$	224.714	IRAM 30 m	13	1989 Mar 23	80″ × 140″
C^{18}O $J = 2 \rightarrow 1$	219.560	IRAM 30 m	13	1990 Feb 11	67″ × 135″
^{13}C^{18}O $J = 2 \rightarrow 1$	209.419	IRAM 30 m	13	1990 Feb 13	...
		S106			
CO $J = 14 \rightarrow 13$	1611.792	KAO	64	1990 Sep	...
CO $J = 6 \rightarrow 5$	691.473	JCMT	8	1989 Jul	...
^{13}CO $J = 6 \rightarrow 5$	661.067	JCMT	8	1990 Jul	...
		M17, W51, Cepheus A, B335			
CO $J = 6 \rightarrow 5$	691.473	JCMT	8	1990 Jul	one-dimensional cuts
^{13}CO $J = 6 \rightarrow 5$	661.067	JCMT	8	1990 Jul	one-dimensional cuts
^{13}CO $J = 2 \rightarrow 1$	220.399	JCMT	22	1990 Jul	one-dimensional cuts
		W49N, S140, DR 21, LkHα 234			
^{13}CO $J = 6 \rightarrow 5$	661.067	JCMT	8	1990 Jul	...

[a] From Paper I.

Absolute line frequencies were especially important for this study of narrow lines, so we made a series of laboratory absorption cell and astronomical measurements to find a precise value (692.9512 GHz) of the HCOOH submillimeter laser local oscillator frequency we use for the ^{12}CO $6 \rightarrow 5$ line. We obtained identical results when we reobserved the ^{12}CO $6 \rightarrow 5$ toward NGC 2024 FIR 5 in 1991 December after carefully verifying the receiver and backend spectrometer frequencies. This, combined with a very different "off" position approximately 10 arcmin from the source, eliminated any possibility of a line shift due to tuning or chopping errors. We estimate our absolute velocity calibration to be correct within less than 0.5 km s^{-1}.

Receiver temperatures measured at the telescope were 2500 K (DSB) for the CO $J = 6 \rightarrow 5$ line and 3500 K (DSB) for ^{13}CO $J = 6 \rightarrow 5$ and CO $J = 7 \rightarrow 6$. Pointing and focus were frequently checked with the UKT14 bolometer (JCMT) or optically (UKIRT). We estimate that the maximum pointing error on both telescopes is typically $\pm 3''$. On both telescopes we observed in double beam switched (sky-chopped) mode with chop throws of 2′ at JCMT and 3′ at UKIRT.

TABLE 2

SOURCE POSITIONS

Source	R.A. (1950)	Decl. (1950)
NGC 2024	5^{h}39^{m}12^s.8	−1°57′04″
W51 IRS 2	19 21 22.4	14 25 13
M17	18 17 34.5	−16 13 24
W49N	19 07 49.9	9 01 17
Cepheus A	22 54 19.1	61 45 43
S140	22 17 42.0	63 03 45
DR 21	20 37 14.0	42 09 00
S106	20 25 33.8	37 12 50
LkHα 234	21 41 57.1	65 53 09
B335	19 34 35.3	7 27 24

The MPE/UCB far-infrared imaging Fabry-Perot interferometer (FIFI; Poglitsch et al. 1991) was used on the Kuiper Airborne Observatory (KAO) to observe the CO $J = 14 \rightarrow 13$ transition. FIFI was equipped for the first time with a high-resolution Fabry-Perot, yielding a velocity resolution of better than 10 km s^{-1}. In order to avoid calibration uncertainties in this new observing mode (due to unknown leakage etc.), we calibrated the spectrum to reproduce the integrated intensity of the low-resolution spectrum published by Harris et al. (1987b). The calibration uncertainty is thus the same as quoted there, i.e., 30%. The chop throw used at the KAO was 4′.5.

The low-J CO observations—up to CO $3 \rightarrow 2$—were carried out at the JCMT and at the IRAM 30 m telescope on Pico Veleta/Spain employing facility receivers. The data were calibrated using the observatories' standard calibration procedures except for the $J = 3 \rightarrow 2$ data. In addition to the standard procedure, the JCMT ^{13}CO $3 \rightarrow 2$ spectra were corrected for sideband imbalance due to the strong atmospheric absorption feature at 325 GHz. The correction procedure was checked by comparing observations made in both sidebands. At 330 and 350 GHz the main beam efficiency of the IRAM 30 m telescope depends on the source size. This is due to deviations from the diffraction limited beam shape, occurring at high frequencies (Baars et al. 1989). The main beam efficiency we use for the calibration of the IRAM ^{12}CO and ^{13}CO $J = 3 \rightarrow 2$ lines is calculated to match the ^{13}CO $J = 3 \rightarrow 2$ intensity measured at JCMT. All low-J line data were taken in position-switched mode typically using a reference position 10′ to the west of the map center.

The C^{18}O $J = 2 \rightarrow 1$ and the ^{13}CO $J = 3 \rightarrow 2$ maps of NGC 2024 were recorded simultaneously. The pointing offset between the two receivers was smaller than 2″. In order to

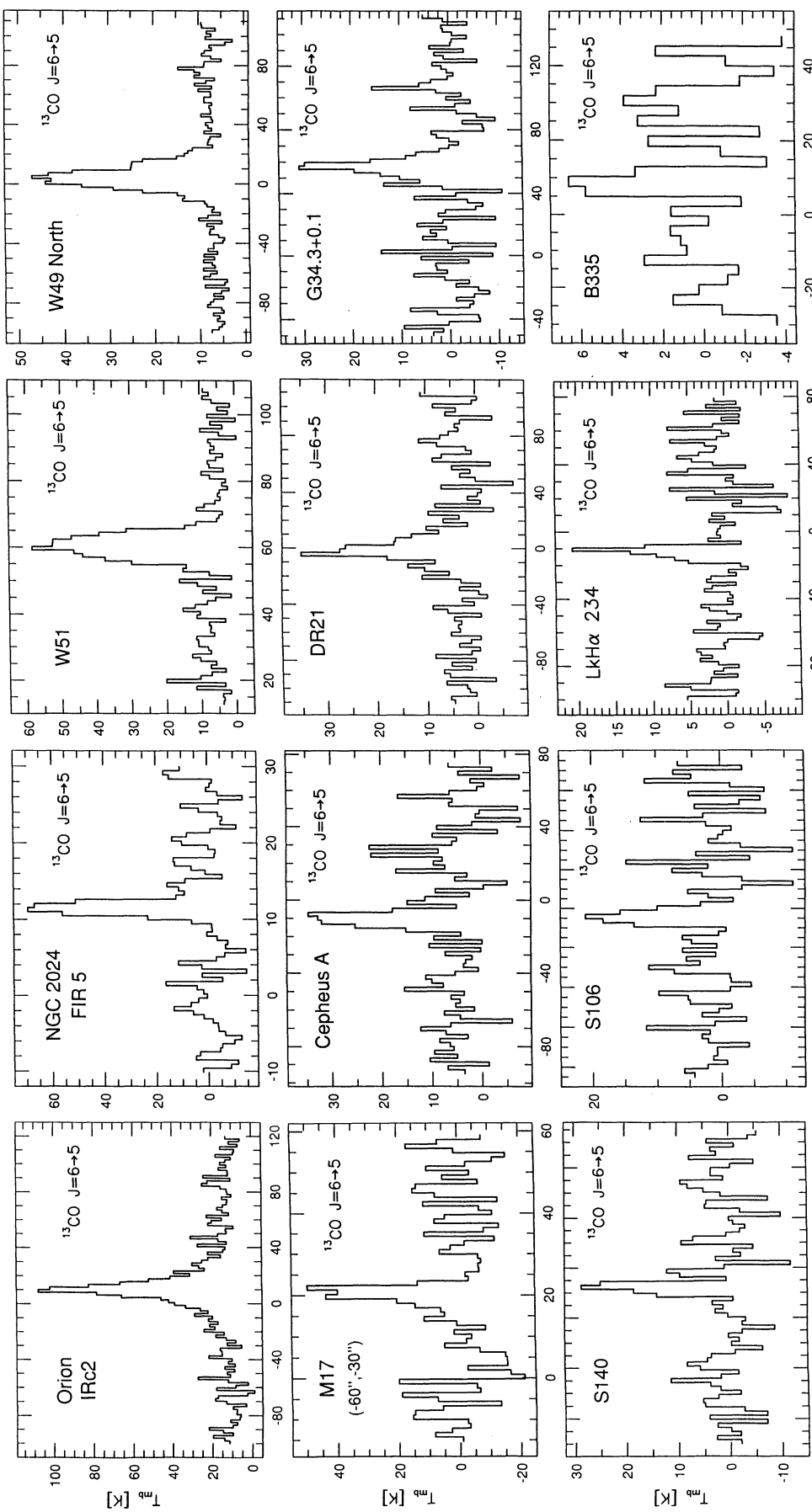

FIG. 1.—Representative ^{13}CO $J = 6 \rightarrow 5$ spectra from all sources detected in this transition up to date. The first two panels (Orion and NGC 2024) are taken from Paper I. Source coordinates are listed in Table 2.

correct for pointing drifts due to thermal effects—the two maps were recorded during sunset—we shifted both maps by 10″ to the W. This shift produces the best agreement between the $C^{18}O$ $J = 2 \rightarrow 1$ data and the $C^{17}O$ $J = 2 \rightarrow 1$ map, which was taken under stable pointing conditions.

3. RESULTS

We found strong ^{12}CO and ^{13}CO $J = 6 \rightarrow 5$ emission from every star-forming region we observed. ^{13}CO $J = 6 \rightarrow 5$ emission was detected not only from the luminous massive star-forming regions, but also from sources of lower luminosity, e.g., LkHα 234 ($L_{IR} = 1200\ L_{\odot}$; Harvey, Wilking, & Joy 1984) and B335 ($L_{IR} = 2.6\ L_{\odot}$; Chandler et al. 1990).

Peak main beam brightness temperatures in the ^{13}CO $J = 6 \rightarrow 5$ line range from 70 K (in NGC 2024) to 5 K (in B335). Table 3 lists the observed line parameters, and spectra are shown in Figure 1. In most sources the main beam brightness temperature of the isotopic line is within a factor of 2 of the ^{12}CO $J = 6 \rightarrow 5$ line. The high $^{13}CO/^{12}CO$ intensity ratios indicate that the main isotope is optically thick in all observed sources.

Based on its line width, the ^{13}CO $6 \rightarrow 5$ emission arises almost exclusively in quiescent gas ($\Delta v < 10$ km s^{-1}). The rare isotopic lines, both submillimeter and millimeter, are generally narrower than the ^{12}CO lines. In most sources this may be attributed to the higher optical depth in the main isotope line. Only DR 21 and W49 also have broader ^{13}CO $J = 6 \rightarrow 5$ components probably emitted by outflowing material.

The results section is split into three main parts. In the first section we derive physical parameters in the star formation regions S106, M17, Cepheus A, and W51. The first three sources have both high UV fluxes and very narrow submillimeter line widths, while W51 has an additional broad line width component. Conditions in these sources form a representative set of physical conditions in luminous star formation regions and provide a basis for comparisons. The second and third sections are parts of the detailed study of the star formation region NGC 2024, resulting in a three-dimensional model for this source. Understanding the structure of the typical star formation region enables us to correct for systematic observational effects, such as self-absorption in the source. The first of the NGC 2024 sections describes maps in a number of lines that successively peel away layers along the line of sight. The second of these sections uses line shapes from even rarer isotopic lines to find the line-of-sight structure toward the protostar candidate FIR 5.

TABLE 3

SUMMARY OF MID- AND HIGH-J CO OBSERVATIONS

Source	T_{mb} (K)	v_{LSR} (km s^{-1})	Δv (km s^{-1})
^{13}CO $J = 6 \rightarrow 5$			
Orion (IRc2)[a]	100	10.1	7.7
NGC 2024	69	11.5	2.0
W51 IRS 2	51	60.3	8.3
M17	48	20.8	3.3
W49 North	41	4.2	16.3
Cepheus A	32	−10.3	8.4
S140	29	−7.7	4.7
DR 21[a]	27	−4.1	5.2
S106	22	−4.8	6.8
LkHα 234	21	−10.8	4.2
B335	6	9	6
^{12}CO $J = 6 \rightarrow 5$			
W51 IRS2	59	57.2	12.2
M17	75	20.7	6.6
S106	73	−4.7	10.2
LkHα 234	22	−10.0	7.4
B335	5	7.9	7.8
^{13}CO $14 \rightarrow 13$			
S106	3	−5	<10

NOTE.—These lines are mostly emitted by quiescent gas ($\Delta v < 10$ km s^{-1}).

[a] Line has prominent wings; Δv refers to the narrow line component.

3.1. *Submillimeter* CO *Emission*

3.1.1. *S106*

In S106 the main beam brightness temperature ratio of the ^{13}CO to ^{12}CO $J = 6 \rightarrow 5$ is 0.3 (22 and 73 K, respectively; Fig. 2 and Table 3), corresponding to $\tau(^{13}CO\ 6 \rightarrow 5) \approx 0.4$ in a single-component, homogeneous cloud model. This implies an optical depth in the main isotope line of ≥ 24 assuming a $^{12}CO/^{13}CO$ abundance ratio of 67 (Langer & Penzias 1990). Assuming a cloud of uniform temperature, this value is a strict lower limit, applicable if both isotopic lines come from exactly the same region; in fact, the filling factor of the main isotope is likely to be greater than that of the rarer isotopes. Both lines agree well in center velocity (4.8 km s^{-1}), suggesting that there are no strong velocity gradients along the line of sight, which could shift the center of the optically thin ^{13}CO line with respect to the optically thick ^{12}CO transition. The velocity

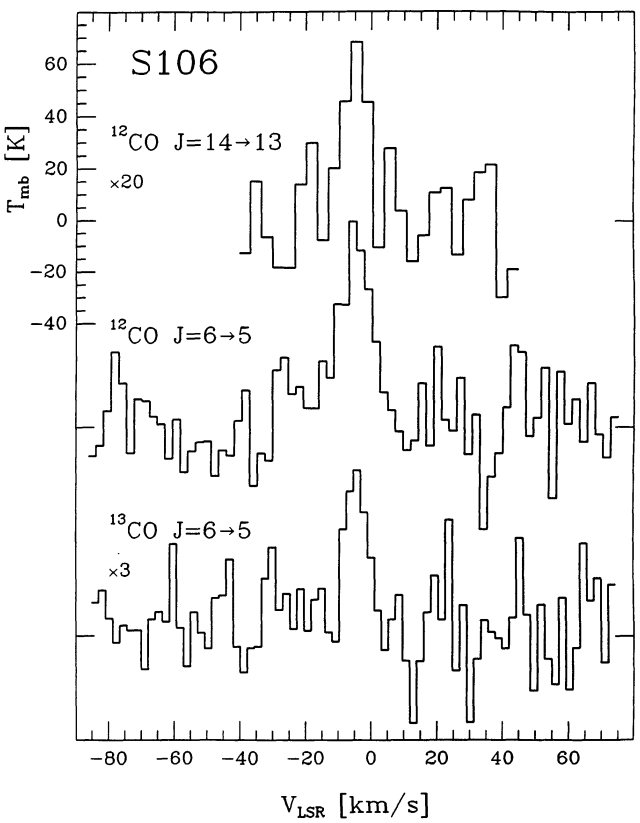

FIG. 2.—Mid- and high-J CO lines observed toward S106. Note in particular that the $J = 14 \rightarrow 13$ line is as narrow as the mid-J lines.

width of the ^{12}CO $J = 6 \rightarrow 5$ line is a factor of 1.5 higher than the width of the isotopic transition (10.2 vs. 6.8 km s^{-1}).

In order to obtain good constraints on the density of the warm gas component in S106, we also measured the ^{12}CO $14 \rightarrow 13$ transition (Fig. 2). Although the line is not fully resolved, it is fairly clear that the high-excitation transition is emitted by the same quiescent gas as the two mid-J lines. Within the measurement accuracy, the line center velocity agrees with the $J = 6 \rightarrow 5$ center velocities. The CO $J = 14 \rightarrow 13$ line width is likely to be somewhat smaller than the measured upper limit of 10 km s^{-1}, since this high-J transition is probably optically thin. Due to the larger KAO beam size, the measured line intensity is likely to underestimate the intrinsic intensity (§ 4.1).

3.1.2. *M17*

The optical depth of the mid-J CO lines toward M17 is even higher than in S106. The $^{13}CO/^{12}CO$ main beam brightness temperature ratio of 0.64 (Table 3) implies $\tau(^{13}CO\ 6 \rightarrow 5) > 1$. While the center velocities of both lines are identical (21 km s^{-1}), the ^{12}CO line is about twice as wide as the ^{13}CO line. This can be explained by the high optical depth in the main isotope line [$\tau(^{12}CO\ 6 \rightarrow 5) \geq 67$]. A microturbulent cloud with this high optical depth would produce a flat-topped line which is not compatible with the observed line shape (Fig. 3). We therefore assume a macroturbulent cloud, where the larger line width in the main isotope is due to the contribution from the few fast-moving cloudlets (Martin, Sanders, & Hills 1984). In this picture the intrinsic line width of individual cloudlets has to be even smaller than the observed ^{13}CO $J = 6 \rightarrow 5$ width of 3.3 km s^{-1}, showing that the mid-J lines are emitted by very quiescent gas.

We also measured the variation of the line intensity across the molecular cloud/H II region interface in M17. We observed six positions along a linear cut perpendicular to the edge-on ionization front in M17 (Fig. 4) similar to the CO $J = 7 \rightarrow 6$ cut obtained by Stutzki et al. (1988) with a larger beam (40″). Both $J = 6 \rightarrow 5$ lines show the same behavior: moving from the H II region into the molecular cloud the mid-J CO intensity rises sharply to its maximum value, marking the edge of the cloud. Further away from the H II region it drops rapidly; within 1′ (0.6 pc at a distance of 2.2 kpc; Chini, Elsässer, & Neckel 1980), the intensity decreases to about 50% of the peak level. The ^{13}CO $J = 2 \rightarrow 1$ line, which we measured for comparison (Fig. 4), peaks further away from the H II region and drops off more slowly than the mid-J lines.

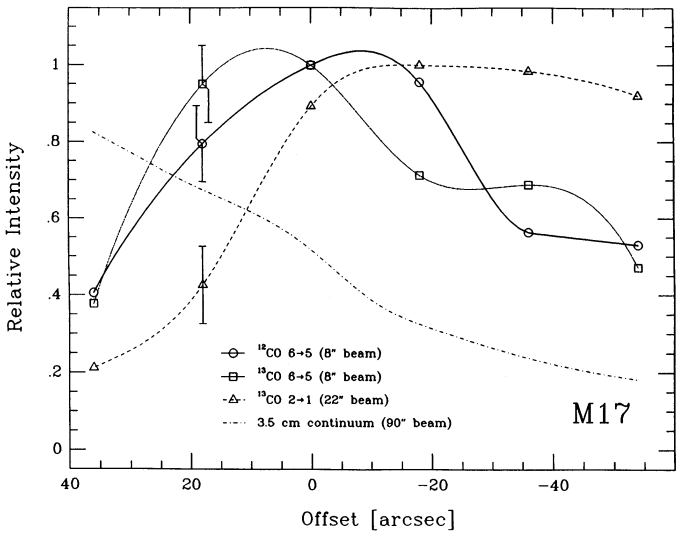

FIG. 4.—CO intensity cuts across the ionization front in M17. The offsets refer to the CO $J = 7 \rightarrow 6$ peak [(−60″, −30″) from our base position in Table 2; Stutzki et al. 1988] and are measured along the line defined by $\Delta\alpha = -1.5 \times \Delta\delta$ (P.A. = 56°.3). The radio continuum measurement is taken from Wilson et al. (1979).

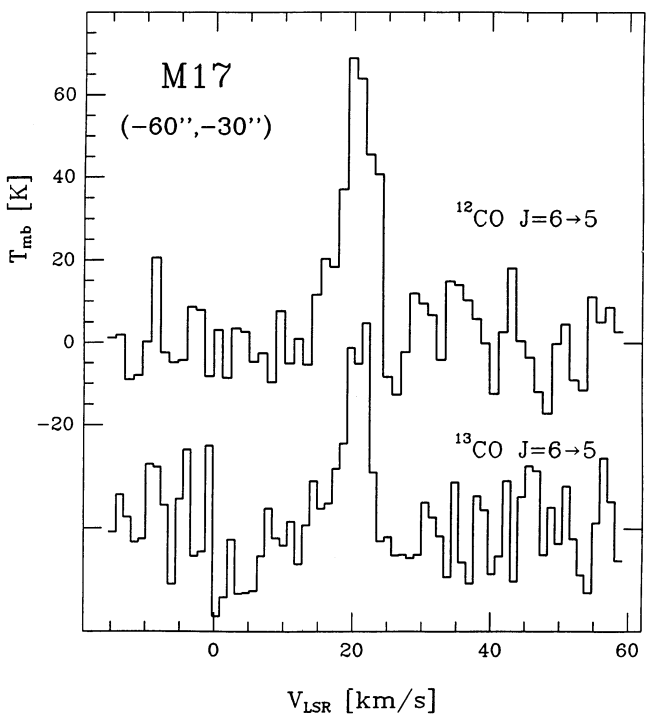

FIG. 3.—Mid-J CO lines observed toward M17. The high $^{13}CO/^{12}CO$ line ratio implies very optically thick emission from the main isotope.

3.1.3. *Cepheus A*

A qualitatively similar relationship between the radio continuum emission and the ^{13}CO $J = 6 \rightarrow 5$ emission is found in

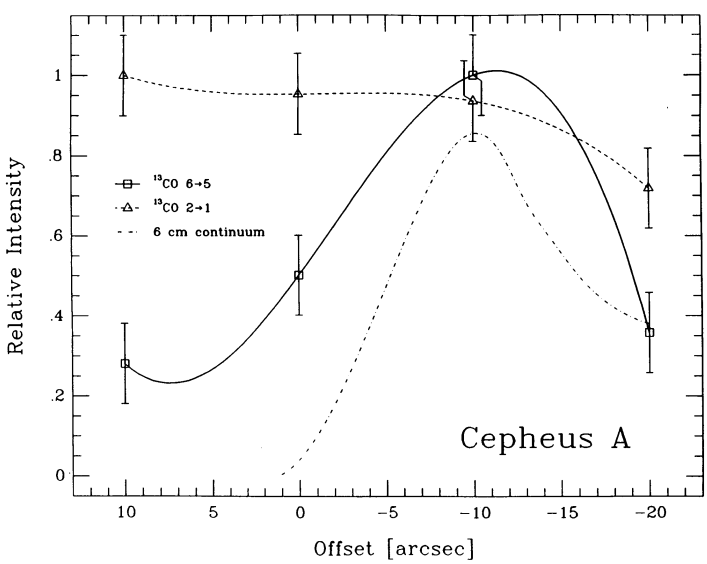

FIG. 5.—CO intensity cuts through the radio continuum peak in Cepheus A. The offsets are measured in declination relative to the position in Table 2. The radio continuum measurement is taken from Rodríguez & Cantó 1983.

Cepheus A, although the linear scale is smaller than in M17. Figure 5 shows an E-W cut measured across the 6 cm continuum peak (Rodríguez & Cantó 1983). The molecular line emission is localized immediately around the H II region. Since the molecular cloud/H II region interface in Cepheus A is seen approximately face-on, the molecular line emission extends to both sides of the radio continuum peak in contrast to the single-sided emission profile in M17's edge-on interface.

The FWHM of the ^{13}CO $J = 6 \rightarrow 5$ emission peak is 20″, corresponding to 0.07 pc at an assumed distance of 700 pc. As in M17, the ^{13}CO $J = 2 \rightarrow 1$ emission seems to be less peaked than ^{13}CO $J = 6 \rightarrow 5$, although the low-J measurement is smeared due to its larger beam width (Fig. 5).

3.1.4. *W51*

A spatial extent of the mid-J CO emission similar to the one found in M17 is measured toward W51 IRS 2 (Fig. 6). In the cut from W51 IRS 2 through W51 IRS 1 to a position south of W51 MAIN the ^{13}CO $J = 6 \rightarrow 5$ line shows a narrow peak centered on IRS 2 with a FWHM of 36″ (1.3 pc at a distance of 7 kpc). Thus it closely follows the radio continuum emission from the compact H II region IRS 2. The ^{13}CO $6 \rightarrow 5$ emission has a minimum about 30″ SE of IRS 2 and rises to a second peak around the maser positions south of W51 MAIN. The secondary peak is almost as strong as the emission toward IRS 2, but is the much wider (FWHM $\approx$ 60″, corresponding to 2.2 pc). Also in this part of the cut, the molecular line emission is coincident with strong 6 cm continuum emission. However, in contrast to the IRS 2 region, the CO emission is not distributed symmetrically around the radio source. The radio peak is offset to the NW of the molecular line peak. Only relatively weak (15% of the peak intensity) 6 cm emission is underlying the main part of the molecular emission maximum. This supports the interpretation as a nearly edge-on molecular cloud/H II region interface (Genzel et al. 1982).

The ^{12}CO $J = 6 \rightarrow 5$ emission profile, which we measured along the same cut, shows only part of the structure seen in the isotopic line. While the main peak centered on W51 IRS 2 looks about the same in both isotopes, the secondary peak in the IRS 1 region is barely visible in ^{12}CO $6 \rightarrow 5$. A comparison of the line profiles shows that this is most likely due to foreground absorption in the main isotope. In Figure 7 we show spectra of different ^{12}CO and ^{13}CO transitions. At LSR velocities higher than 62 km s^{-1} the ^{12}CO $6 \rightarrow 5$ line is weaker than the isotopic ^{13}CO $6 \rightarrow 5$ line. This is possible only if the main isotope emission is absorbed by colder foreground gas. Comparing the ^{12}CO $6 \rightarrow 5$ line with the ^{12}CO $J = 2 \rightarrow 1$ line shows that the absorption occurs at the same velocity as in the low-J lines, i.e., that it is most likely due to the known foreground gas centered at v_{LSR} = 64 km s^{-1} (Phillips et al. 1981). Since the absorption covers all of the higher velocity emission of ^{12}CO $J = 6 \rightarrow 5$ ($v_{LSR} > 62$ km s^{-1}) the line appears to be shifted to lower velocities (v_{LSR} = 57 km s^{-1}) with respect to the isotopic ^{13}CO $J = 6 \rightarrow 5$ line (v_{LSR} = 60 km s^{-1}) which is not affected by the absorption.

Since the absorbing foreground material is cold (White et al. 1986), its optical depth should rapidly become smaller for higher transitions. In fact the ^{12}CO $J = 7 \rightarrow 6$ line (Jaffe et al. 1987; Fig. 7) is barely affected. Only the slight asymmetry of the line and its low center velocity of v_{LSR} = 59 km s^{-1} reveal the effects of a weak foreground absorption. The weaker self-absorption also explains why the ^{12}CO $J = 7 \rightarrow 6$ line appears to be stronger than the $6 \rightarrow 5$ transition despite the fact that it should rather be weaker due to a lower beam filling in the 32″ IRTF beam.

With the measured main beam brightness temperatures of

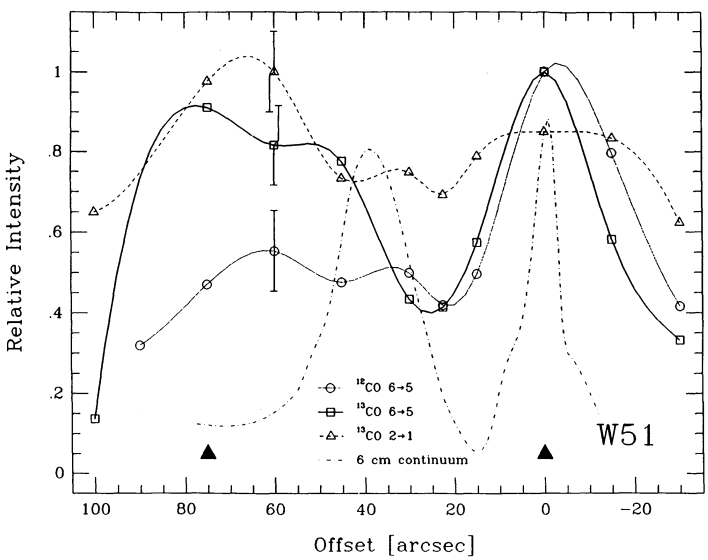

FIG. 6.—CO intensity cuts from W51 IRS 2 to W51 MAIN. The offsets refer to the IRS 2 position given in Table 2 and are measured along the line defined by $\Delta\delta = -0.75 \times \Delta\alpha$ (P.A. = 126°9). Maser positions are marked by triangles (Genzel et al. 1982). The radio continuum measurement is taken from Genzel et al. (1982).

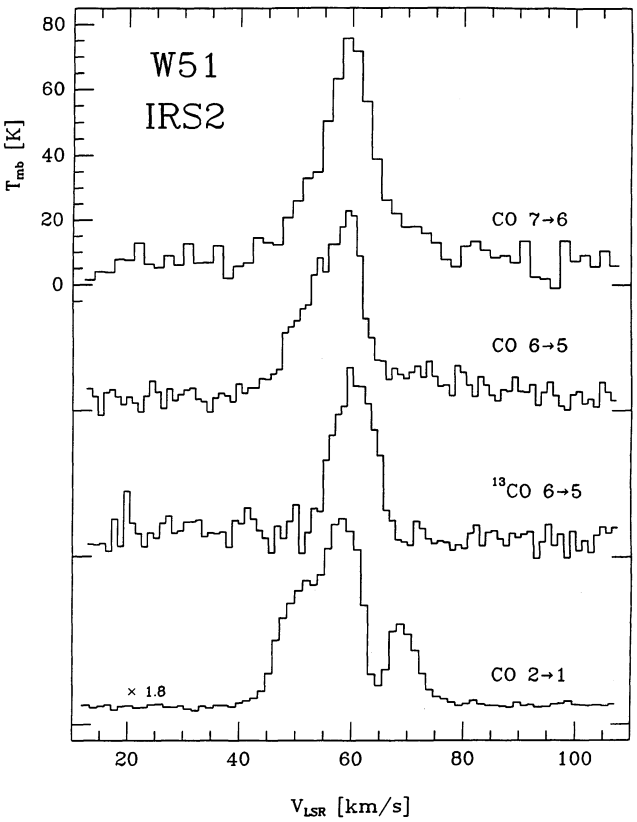

FIG. 7.—CO line shapes observed toward W51 IRS 2. The CO $J = 2 \rightarrow 1$ (from Jaffe et al. 1989) and $J = 6 \rightarrow 5$ lines are clearly affected by absorption in the cold foreground cloud at v_{LSR} = 65 km s^{-1}. The continuum offset in all spectra is real. The CO $J = 7 \rightarrow 6$ line is taken from Jaffe, Harris, & Genzel (1987).

the ^{13}CO and ^{12}CO $J = 6 \rightarrow 5$ lines of 51 K and 59 K, respectively (Table 3), we estimate an optical depth of $\tau \approx 2$ in the isotopic line. However, since the self-absorbed ^{12}CO line is likely to have an intrinsic line temperature of $T_{mb} \geq 70$ K (the main beam brightness temperature of the ^{12}CO $J = 7 \rightarrow 6$ line, measured with a larger beam), the ^{13}CO $J = 6 \rightarrow 5$ optical depth is probably closer to ≈ 1 [1.3 for $T_{mb}(^{12}\mathrm{CO}) = 70$ K].

3.2. *Millimeter and Submillimeter Maps of NGC 2024*

The four maps we present here probe gradually deeper into the cloud, showing different "slices" of the three-dimensional structure of the source. As one observes lines of gradually lower optical depth (^{12}CO $7 \rightarrow 6$, ^{13}CO $3 \rightarrow 2$, C^{18}O $2 \rightarrow 1$, C^{17}O $2 \rightarrow 1$), the surface structure becomes less prominent and the column density distribution in the molecular cloud starts to dominate the maps. According to the standard source model (§ 4.3), the main part of the molecular cloud is located behind the H II region. Our selection of tracers matches the likely temperature profile inside the cloud: the $J = 7 \rightarrow 6$ transition traces the warm gas immediately behind the H II region, whereas the lower-J lines trace progressively cooler material deeper inside the cloud.

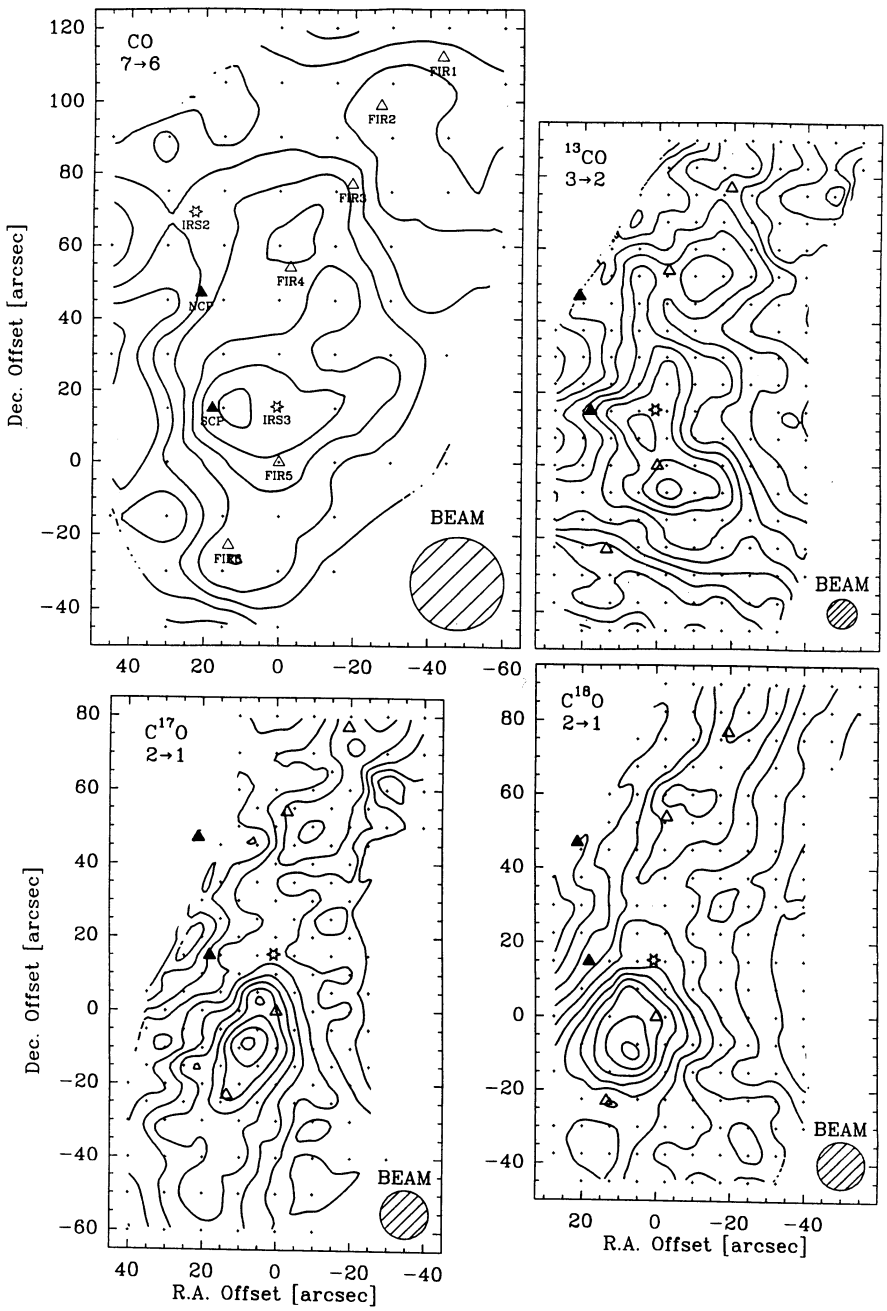

FIG. 8.—Integrated intensity maps of NGC 2024. Contour levels are CO $7 \rightarrow 6$: (35 to 305 by 45) K km s^{-1}, ^{13}CO $3 \rightarrow 2$: (50 to 140 by 9) K km s^{-1}, C^{17}O $2 \rightarrow 1$: (3.5 to 23.5 by 2) K km s^{-1}, C^{18}O $2 \rightarrow 1$: (18 to 78 by 6) K km s^{-1}. Prominent features observed at other wavelengths are marked on each map and labeled in the upper left panel.

Our three low-J isotopic CO maps ($C^{17}O$ $2 \rightarrow 1$, $C^{18}O$ $2 \rightarrow 1$, ^{13}CO $3 \rightarrow 2$; Fig. 8) cover most of the region mapped in the 1.3 mm continuum by Mezger et al. (1988). Mezger et al. (1988) found a number of clumps (denoted FIR 1–6) which they interpret as cold protostellar condensations embedded in the dense ridge. Our low-J isotopic CO measurements, which should be most sensitive to the molecular emission from these clumps, show the same basic structure as the millimeter dust continuum (Fig. 9). The emission arises from a N-S extended ridge with a series of embedded emission peaks. The counterparts of the dust peaks FIR 3 and FIR 4 are clearly seen in the $C^{18}O$ and $C^{17}O$ $J = 2 \rightarrow 1$ maps. The emission minimum along the chain of FIR peaks lies between FIR 4 and FIR 5, again in good agreement with the mm continuum. The main difference between the latter and our $J = 2 \rightarrow 1$ maps is that FIR 5 and FIR 6 do not appear as two individual peaks in the molecular line emission but seem to be part of one entity peaking between the positions of the continuum peaks. Furthermore, the intensity contrast between the peaks and the surrounding region in our molecular line maps is lower than in the millimeter continuum. Nevertheless, the good overall agreement between the low-J emission of rare CO isotopes and the optically thin millimeter continuum indicates that the molecular lines largely trace the same material as the dust measurements.

Although the ^{12}CO $J = 7 \rightarrow 6$ emission generally follows the

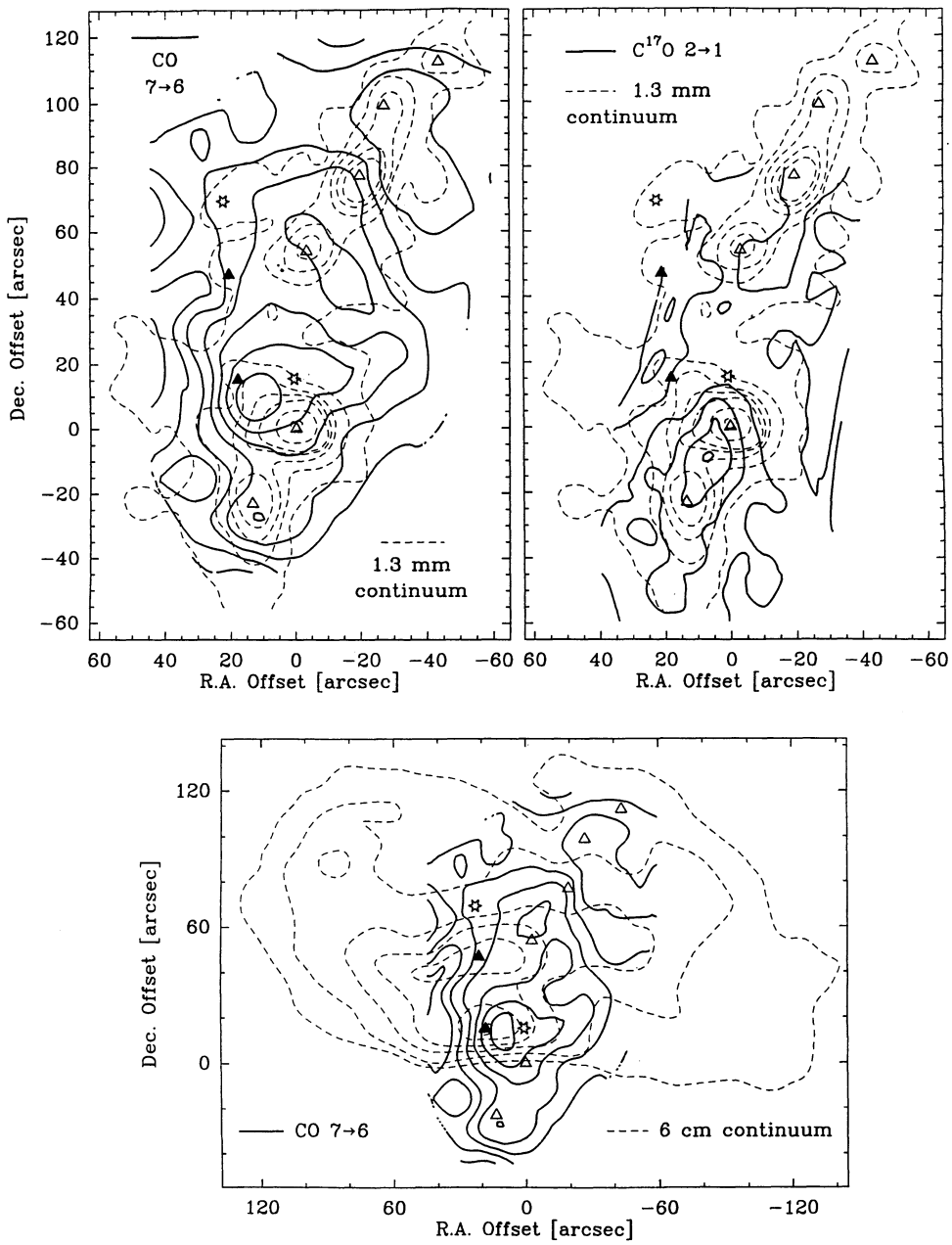

FIG. 9.—Overlays of maps taken toward NGC 2024. *Top left*: CO $7 \rightarrow 6$ and 1.3 mm continuum (Mezger et al. 1988); *top right*: $C^{17}O$ $2 \rightarrow 1$ and 1.3 mm continuum; *bottom*: CO $7 \rightarrow 6$ and 6 cm continuum (Crutcher et al. 1986).

N-S extended molecular ridge, this map shows a number of additional features. It peaks north of FIR 5, where the low-J isotopic CO maps show an emission minimum. The peak is approximately coincident with the southern compact peak (SCP; Crutcher et al. 1986) of the 6 cm continuum emission from the H II region and with IRS 3 (Barnes et al. 1989) an infrared point source which may be related to the SCP. Also in the northern part the ^{12}CO $J = 7 \rightarrow 6$ emission reflects features connected with the H II region : in the NW the $7 \rightarrow 6$ map extends toward the region around the northern compact peak (NCP; Crucher et al. 1986) and IRS 2 (Grasdalen 1974) which is probably one of the exciting stars of the H II region.

From the ^{13}CO $J = 6 \rightarrow 5$ measurements presented in Paper I [$\tau(^{13}\mathrm{CO}\ 6 \rightarrow 5) \approx 1$], it is clear that ^{12}CO $7 \rightarrow 6$ is very optically thick when averaged over all source components. This transition therefore does not trace the column density of the molecular material but reflects the temperature distribution at the front surface of the molecular cloud. Hence, the structure seen in the ^{12}CO $J = 7 \rightarrow 6$ map is determined by the location of the heating sources which are most likely coincident with the emission peaks in the H II region in front of the molecular ridge (Fig. 9).

The CO $J = 7 \rightarrow 6$ map suggests that the dense molecular ridge with the embedded FIR clumps is very close to the molecular cloud/H II region interface. If the dense N-S ridge were embedded deeply inside a more extended molecular cloud, the very optically thick CO $7 \rightarrow 6$ line map would not show the ridge structure. The dense material has to be within an optical depth of ≈ 1 from the molecular cloud surface in order to be visible in this transition. For a homogeneous gas density of $n_{\mathrm{H_2}} \geq 10^5$ cm^{-3}, $\tau(^{12}\mathrm{CO}\ 7 \rightarrow 6) = 1$ is reached at a depth of ≤ 0.003 pc inside the cloud. Although this estimate is rather crude and does not take clumpiness into account, it indicates that the dense molecular ridge is in the immediate vicinity of the H II region.

CO $J = 7 \rightarrow 6$ spectra taken at $\Delta\alpha = \pm 90''$ show that the mid-J CO emission extends over $\geq 3'$ in right ascension (Fig. 10). This indicates that the warm molecular gas reaches about as far as the 30% contour of the 6 cm radio continuum, although only the central N-S ridge has enough column density to be prominent in transitions of rare CO isotopes. At a distance of 1.5 away from the molecular ridge also the densities are probably too low to thermalize density tracing lines, and trapping is likely to play an important role in the excitation of the ^{12}CO $7 \rightarrow 6$ transition.

The ^{13}CO $J = 3 \rightarrow 2$ map provides a link between the ^{12}CO $J = 7 \rightarrow 6$ map and the isotopic $J = 2 \rightarrow 1$ maps. Although this map is dominated by the material in the N-S ridge, it also shows strong emission around SCP and IRS 3 and an extension toward NCP. Its peak is close to FIR 5 and part of an EW extension following the southern edge-on ionization front seen in the radio continuum.

3.3. *Line Shapes toward FIR 5*

In order to reveal the line of sight structure toward the millimeter continuum peak FIR 5 we obtained spectra in nine different CO lines (Figs. 11, 12; Table 4). Accurate estimates of column densities, temperatures, and relative locations of the line-of-sight components can be obtained by modeling line center shifts and the clear self-absorptions. The source structure plays a critical role in interpreting line and continuum emission from such a complicated region.

The most striking difference among the nine transitions we observed is that all the isotopic lines peak at $v_{\mathrm{LSR}} = 11$ km s^{-1}, whereas the maxima of the three ^{12}CO lines are close to 13 km s^{-1}. Similar to the situation in W51, this apparent velocity shift is most likely caused by foreground absorption in the ^{12}CO lines, as can be seen from an analysis of the optically thin isotopic lines (Fig. 11). In addition to the 11 km s^{-1} peak, all but the ^{13}CO lines show a secondary maximum at $v_{\mathrm{LSR}} = 9$ km s^{-1}. The double-peaked shape of the very rare isotope ^{13}C^{18}O $J = 2 \rightarrow 1$ line suggests that this is due to two emissive source components. Indeed, if we correct for the C^{17}O $J = 2 \rightarrow 1$ hyperfine splitting, the intensity ratio between C^{18}O and C^{17}O $J = 2 \rightarrow 1$ is constant across the line profile. This is a clear indication that we are seeing two optically thin emission components. The ^{13}CO $J = 3 \rightarrow 2$ line is not double-peaked, but it shows the 9 km s^{-1} component as a shoulder on the low-velocity side of the line.

The component centered at $v_{\mathrm{LSR}} = 11$ km s^{-1} is warm and dense, since it contributes all of the ^{13}CO $J = 6 \rightarrow 5$ emission (Fig. 11), whereas the 9 km s^{-1} component is cold. It is only prominent in the lines up to $J = 3 \rightarrow 2$. In order to produce the strong isotopic CO emission both components need a con-

TABLE 4.

PARAMETERS OF NINE LINES OBSERVED TOWARD NGC 2024 FIR 5

TRANSITION	MAXIMUM		SECOND MAXIMUM		CENTRAL DIP		$\frac{[^{12}C^{16}O]}{[^{x}C^{y}O]}$
	T_{mb} (K)	v_{LSR} (km s^{-1})	T_{mb} (K)	v_{LSR} (km s^{-1})	T_{mb} (K)	v_{LSR} (km s^{-1})	
Main Isotope							
CO $7 \rightarrow 6$	77.3	12.8	...		...		1
CO $6 \rightarrow 5$	45.2	13.5	...		...		1
CO $3 \rightarrow 2$	28.7	13.0	13.2	7.9	2.0	9.5	1
Rare Isotopes							
^{13}CO $6 \rightarrow 5$	68.5	11.5	...		...		67
^{13}CO $3 \rightarrow 2$	62.2	11.2	...		...		67
C^{18}O $2 \rightarrow 1$	18.9	11.1	13.9	9.2	9.3	10.0	450
C^{18}O $1 \rightarrow 0$[a]	4.3	11.2	3.4	9.3	2.3	10.0	450
C^{17}O $2 \rightarrow 1$	3.7	11.3	3.4	9.5	2.8	10.2	2000
^{13}C^{18}O $2 \rightarrow 1$	0.2	11.3	0.2	9.4	0.1	10.2	30000

[a] IRAM 30 m data (26″ beam), courtesy of J. Richer (private communication).

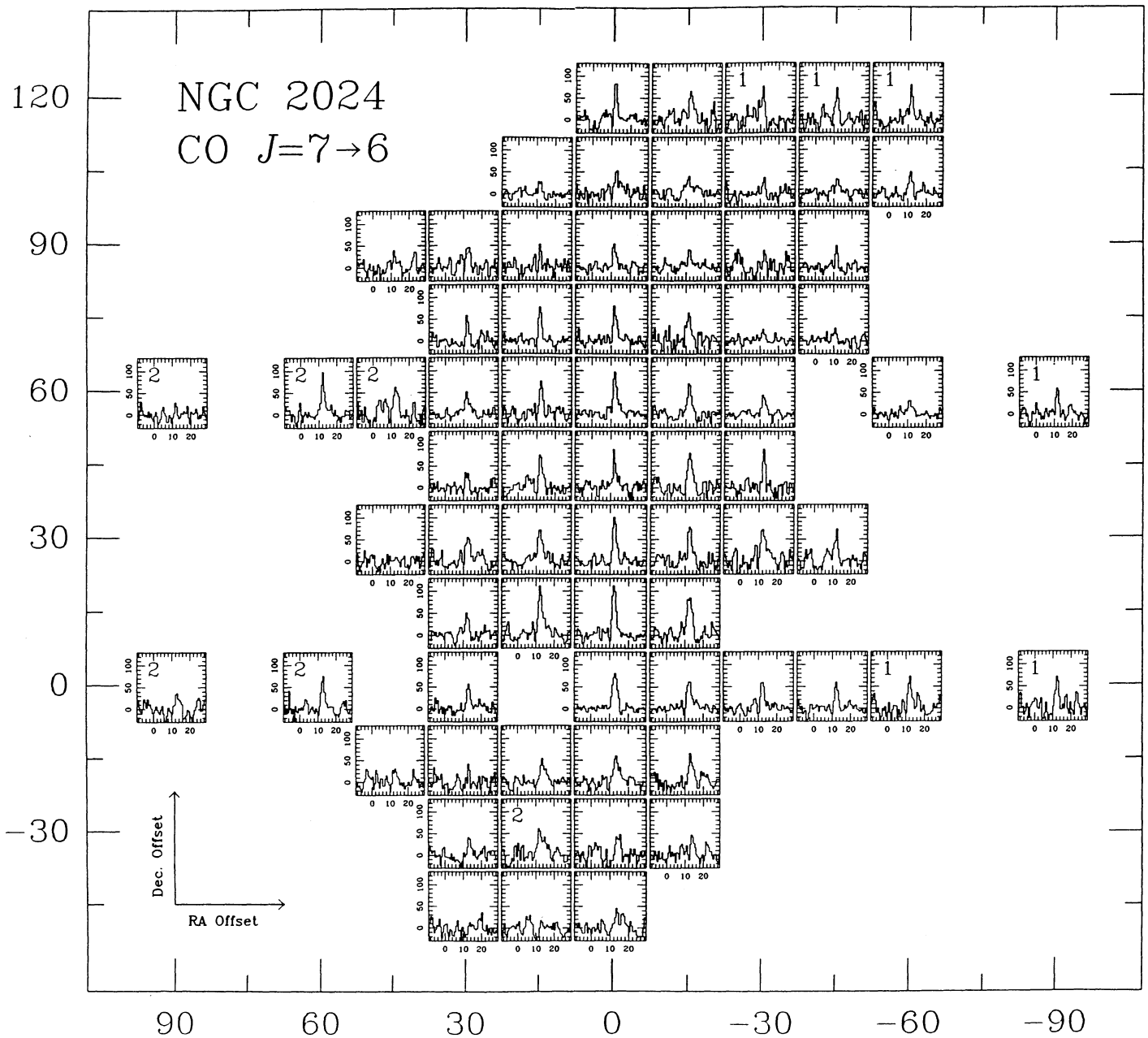

FIG. 10.—CO $J = 7 \rightarrow 6$ spectra measured toward NGC 2024. Offsets are in arcseconds relative to the FIR 5 position (Table 2). Panels labeled in the upper left corner show only data from chop cycles with the reference beam away from the main source in order to avoid effects of self-chopping (chop throw: 180″ EW).

siderable column density. In accordance with the standard source model (§ 4.3), we assume that the 9 km s^{-1} component is located in front of the 11 km s^{-1} component. This geometry explains the apparent velocity shift between the isotopic lines and the main isotope transitions in the same way as in W51 (§ 3.1). Only the higher velocity part of the ^{12}CO background emission is transmitted through the cold, blueshifted foreground material, thus mimicking a redshifted ^{12}CO emission. Isotopic lines, with lower optical depth in the foreground component, are less affected and show the intrinsic background center velocity.

In Paper I we calculated the column density in NGC 2024's warm gas component, using the ^{13}CO $J = 6 \rightarrow 5$ line that traces gas at ≈ 100 K. We found that NGC 2024 contains similarly large amounts of warm quiescent gas as the other massive star-forming regions. In order to understand how this warm gas is related to the cooler material, we now study the physical conditions in this source as traced by low-J CO lines. The large variety of lines we observed in NGC 2024 allows us to distinguish between the two major source components and to calculate accurate physical quantities for the two components individually.

We use the three transitions $C^{18}O$ $2 \rightarrow 1$, $C^{17}O$ $2 \rightarrow 1$, and ^{13}CO $3 \rightarrow 2$ to characterize the physical state of the cooler molecular gas. This will be done by fitting the emission calculated for a physical source model to the three observed lines simultaneously. The $C^{18}O$ and $C^{17}O$ lines are taken from the IRAM maps. The ^{13}CO $3 \rightarrow 2$ line is the one measured at

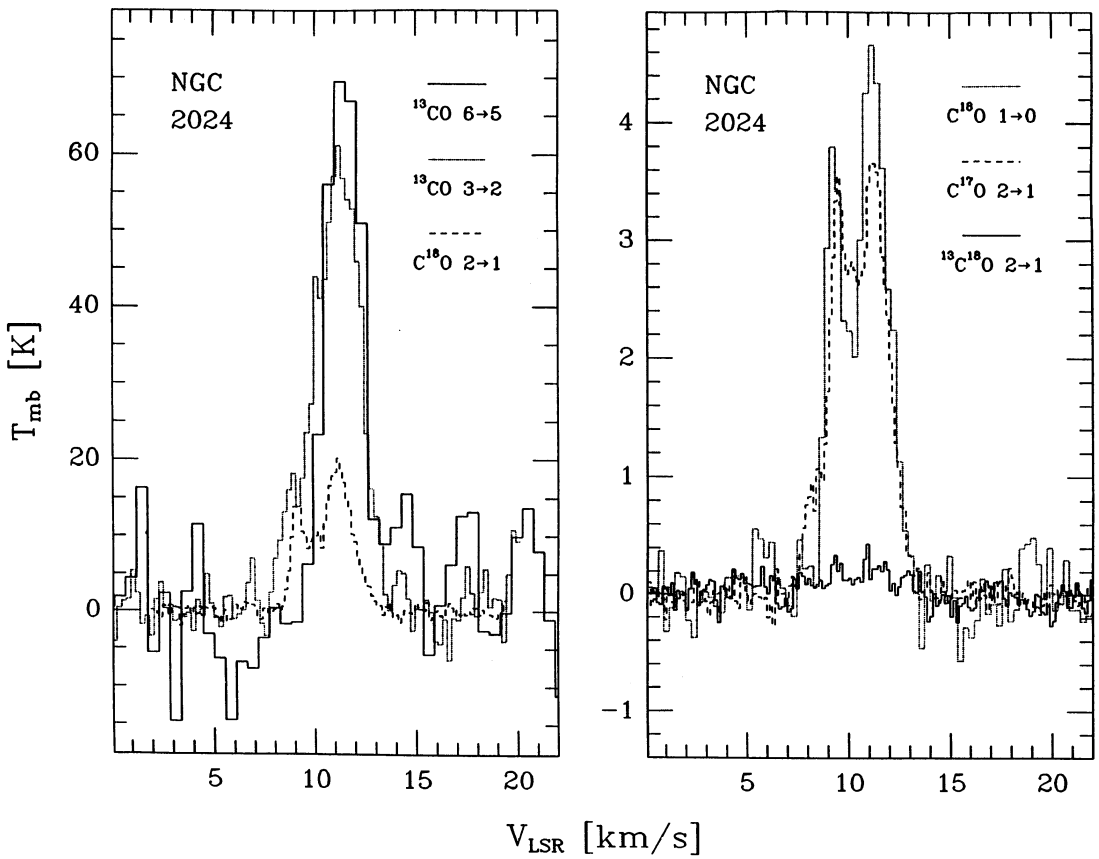

FIG. 11.—Overlay of six isotopic CO lines observed toward NGC 2024 FIR 5. The C^{18}O 1–0 spectrum has been provided by J. Richer (private communication).

JCMT. The JCMT beam at 330 GHz matches the IRAM beam size at 220 GHz very well (15″ and 13″, respectively). All three spectra clearly show the two source components: C^{18}O and C^{17}O $J = 2 \rightarrow 1$ are double-peaked, ^{13}CO $J = 3 \rightarrow 2$ shows a shoulder on the low-velocity side. The source model we fit to the observational data assumes two components, a background component near 11 km s^{-1} and a foreground component near 9 km s^{-1}.

The densities in the background component are well above the critical densities of the transitions considered here (Snell et al. 1984; Schulz et al. 1991). In the foreground the density is lower, ($n_{H_2} \approx 8 \times 10^4$ cm^{-3}; Henkel, Walmsley, & Wilson 1979) but still high enough to thermalize the lower-J CO lines. We therefore assume fully thermalized populations in both components (LTE).

For each of the two source components, the radiation temperature $T_R(v)$ from a given transition is modeled by

$$T_R(v) = T_{R-J}(T_{ex}, v_{rest}) \times \left\{1 - \exp\left[-\tau_0(N_{CO}, T_{ex}) \times \sum_j s_j \phi(v - v_j - v_0)\right]\right\}, \quad (1)$$

where ϕ is the normalized line profile (Gaussian), and $T_{R-J}(T_{ex}, v_{rest})$ is the Rayleigh-Jeans corrected excitation temperature of the transition. The velocity offsets v_j and the relative line strengths s_j are given by the offsets and relative intensities of the nine hyperfine components in the case of the C^{17}O $2 \rightarrow 1$ ($j = 1, \ldots, 9$). For the isotopes that do not show hyperfine splitting, $v_j = 0$ and s_j ($j = 1$) is the relative isotopic abundance[4] multiplied with the excitation ratio between different energy levels at LTE. The two source components are added allowing for absorption of the background emission by the foreground component. The fitting routine varies the following parameters independently for the two source components v_0, the center velocity of the emission (identical for all three lines); Δv, the FWHM of the line profile (identical for all three lines); the CO column density; and T_{ex}, the excitation temperature, which is equal to T_{kin}, assuming LTE.

A two-component model fits the three low-J lines very well (Fig. 13). The fit identifies a cold foreground and a warm background component (Table 5). The background component has the velocity signature that is typical for most molecular emission lines observed in NGC 2024, whereas the foreground component agrees very well with absorption-line measurements. The column densities, both in the foreground and in the background, are very high, implying optically thick low-J emission from all isotopes more abundant than C^{18}O. In the foreground, due to its low kinetic temperature, even C^{18}O $J = 2 \rightarrow 1$ is close to being optically thick.

The background temperature derived from these low-J lines is almost as high as the value obtained in Paper I from the comparison of ^{13}CO $6 \rightarrow 5$ and $3 \rightarrow 2$ (67 vs. 95 K). The column density is only 50% higher than in Paper I. This shows that the warm molecular gas traced by the mid-J lines makes up a dominant fraction of the background material.

[4] Assumed abundances: [CO]/[^{13}CO] = 67; [CO]/[C^{18}O] = 450; [CO]/[C^{17}O] = 2000.

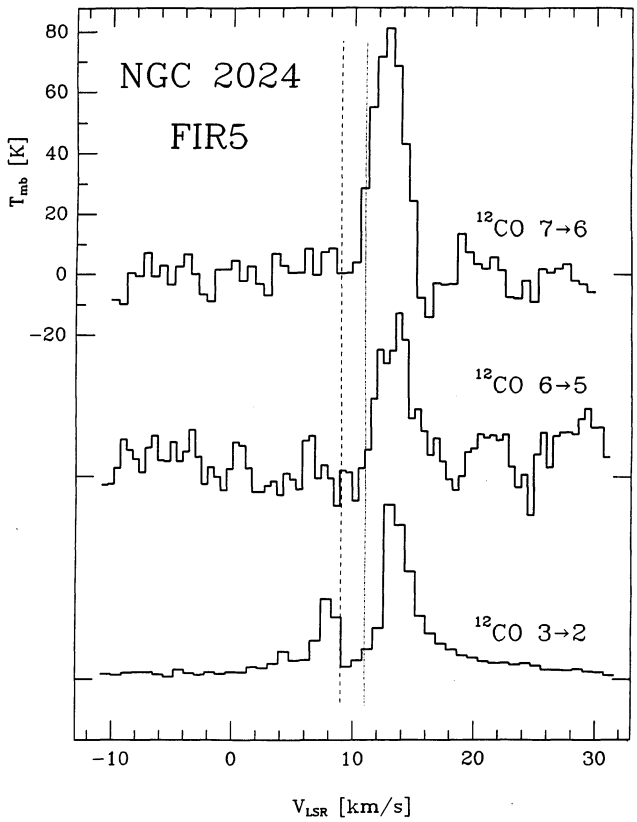

FIG. 12.—CO lines observed toward NGC 2024 FIR 5. The vertical lines mark the positions of the main maxima (*dotted*) and the secondary maxima (*dashed*) of the isotopic CO lines.

In Tables 6 and 7 we compare the column densities inferred by our fit with results obtained by other groups. The difference between our foreground column density value and the infrared extinction measurements is due to the fact that we measured with a small beam toward an absorption peak (FIR 5) where the optical depth in H_2CO is about a factor of 2 higher than toward IRS 2 (Crutcher et al. 1986). Thus, given the methodical differences, there is good agreement between the NIR measurements and the molecular data, indicating that the mean visual extinction in the foreground is between 20 and 30 mag with peak values reaching 60 mag.

Background column densities derived from observations of molecules with more complicated chemistry agree well with our CO measurements, taking the abundance uncertainties into account. Only the values reported by Moore et al. (1989) are about an order of magnitude lower. Their calculation is based on a thermalized population of the CS level. Though trapping may increase the population of the higher levels, the CS $J = 7 \rightarrow 6$ transition is probably quite subthermal. Thus the column density derived from the LTE emission model is likely to underestimate the true CS column density.

Our results confirm the discrepancy between the column density inferred from molecular line observations and the millimeter continuum results of Mezger et al. (1988). The dust column density we cite in Table 7 is calculated for an 11″ beam. We convert the peak flux density from their 1.3 mm map toward FIR 5 ($\approx$4.2 Jy per 11″ beam = 1.3×10^9 Jy sr^{-1}) into a beam-averaged column density by applying the same conversion factor as the authors ($N_{H_2} = 6.6 \times 10^{15}$ cm^{-2} S_{1300}/Ω for 16 K dust). The resulting molecular hydrogen column density lies between the two values given by Mezger et al.: 6.8×10^{23} cm^{-2} (averaged over a 90″ beam; their Table 4) and 3.0×10^{25} cm^{-2} (peak value obtained from a geometrical decomposition of FIR 5; their Table 3).

4. DISCUSSION

4.1. *The Quiescent Warm Gas in Star Formation Regions*

4.1.1. *A Clumpy High-Temperature Component*

Our mid-J CO observations provide estimates of the physical conditions in the warm quiescent gas component in regions of massive star formation. In the limit of unity beam filling, the Planck-corrected main beam brightness temperature of the optically thick ^{12}CO $J = 6 \rightarrow 5$ line sets a lower limit to the kinetic gas temperature. This lower limit is typically around 100 K in bright sources.

The temperature may well be higher than this limit. It is clear that molecular clouds are clumpy down to scale sizes of order of our resolution limit (e.g., Stutzki & Güsten 1990) and probably below. It is therefore likely that a substantial fraction of the material sampled by the telescope beam it at even higher temperatures than the 100 K lower limit in all our sources. The signature of low beam filling is particularly clear when we compare our high-resolution data with data obtained from submillimeter observations made with the 91 cm diameter telescope of the KAO. In the CO $J = 7 \rightarrow 6$ map of NGC 2024 (Fig. 8), observed with a (probably beam-diluted) 25″ beam, the E-W extent of the 50% intensity contour is $\leq$70″. Convolving the map with a Gaussian beam of 98″ FWHM (corresponding to the KAO beam size at 800 GHz; Krügel et al. 1989) reduces the peak intensity by an approximate factor of 2. The increase in line intensity seen in S106 between KAO observations (27 K; Krügel et al. 1989) and UKIRT observations (55 K; Harris et al. 1987b) is also a factor of 2. Low filling factors are also implied by a comparison of our high-resolution data with KAO observations of CO $J = 9 \rightarrow 8$ toward W51 (Boreiko & Betz 1991). This transition is close enough to the $6 \rightarrow 5$ transition that the line temperatures seen in the warm gas component should be comparable. However, the $9 \rightarrow 8$

TABLE 5

BEST-FIT TWO-COMPONENT MODEL FOR THE EMISSION TOWARD NGC 2024 FIR 5

NGC 2024 FIR 5 COMPONENT	FIT PARAMETERS				OPTICAL DEPTHS		
	T_{ex} (K)	v_{LSR} (km s^{-1})	Δv (km s^{-1})	N_{H_2}[a] (cm^{-2})	C^{17}O 2→1	C^{18}O 2→1	^{13}CO 3→2
Foreground	23.5	9.2	0.9	5.4×10^{22}	0.23	1.0	8.7
Background	67.4	11.1	1.8	2.0×10^{23}	0.07	0.3	3.9

[a] Assumes $[C^{17}O]/[H_2] = 4 \times 10^{-8}$.

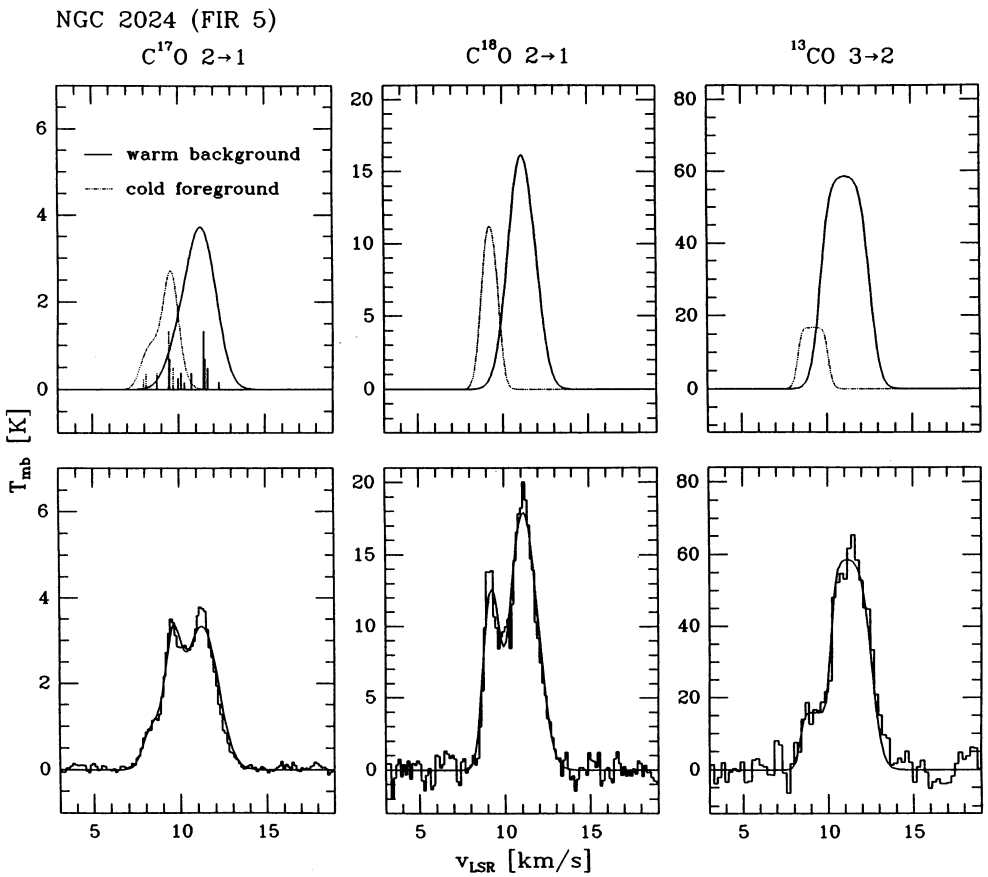

FIG. 13.—Two-component model fit to three low-J CO lines detected toward NGC 2024 FIR 5. The upper panels show the calculated emission from the two source components individually. The two emission components add up to the profiles shown in the lower panels, overlaid by the measured line profiles. The positions and relative intensities of the $C^{17}O$ 2 → 1 hyperfine components are indicated in the upper left panel.

lines observed with the KAO's 80″ beam turn out to be substantially weaker than the 6 → 5 lines from JCMT. Toward W51 IRS 2, for instance, the main beam brightness temperature in CO $J = 9 \rightarrow 8$ is ≈10 K (Boreiko & Betz 1991; T_A^* value divided by the reported main beam efficiency of 0.6[6]) as opposed to the >59 K in the 6 → 5 line (the apparent peak intensity is likely to be affected by foreground absorption; Fig. 7). This difference is readily explained by the cut displayed in Figure 6: The mid-J line emission is strongly peaked toward the compact H II region and fills only a small fraction of the 80″ KAO beam.

In the two low-luminosity sources (B335 and LkHα 234), the average gas temperatures are likely to be lower than in the massive star-forming regions. Minimum temperatures of 15 and 35 K, respectively, are implied by the peak brightness temperatures of the optically thick CO $J = 6 \rightarrow 5$ lines. However, if the kinetic temperature were as low as 15 K, a column density of $N_{H_2} \approx 10^{24}$ cm^{-2} at a density of $n_{H_2} \approx 10^6$ cm^{-3} would be required to explain the ^{13}CO $J = 6 \rightarrow 5$ emission. It seems more likely that we are seeing somewhat warmer gas ($T_{kin} \approx$ 30–50 K) with a low beam filling factor (≈0.1–0.3).

[6] $\eta_{mb} = 0.6$ is derived from Moon measurements and therefore has to be considered as an upper limit.

TABLE 6

COMPARISON OF COLUMN DENSITIES DERIVED FOR THE FOREGROUND MATERIAL

A_v	N_{H_2} (cm^{-2})	Method
57	**5.4 × 10^{22}**	Toward FIR 5, this work; 13″ beam
27	**2.5 × 10^{22}**	H_2CO absorption; VLA, 13″ beam[a]
21.5	2.0 × 10^{22}	Extinction toward IRS 2, NIR speckle interferometry[b]
12	1.1 × 10^{22}	Extinction toward IRS 2, Brackett series[c]
32	3.0 × 10^{22}	Extinction toward IRS 2, NIR photometry[d]

NOTE.—Values in boldface are from the references; conversion between A_v and N_{H_2}: $N_{H_2} = 9.4 \times 10^{20}$ cm^{-2} A_v mag^{-1}.

[a] Crutcher et al. 1986; assumes $[H_2CO]/[H_2] = 10^{-9}$.

[b] Jiang, Perrier, & Léna 1984.

[c] Thompson, Thronson, & Campbell 1981.

[d] Grasdalen 1974.

TABLE 7

COMPARISON OF PEAK COLUMN DENSITIES DERIVED FOR THE BACKGROUND MATERIAL

N_{H_2} (cm^{-2})	Beam	Method
2.0×10^{23}	13″	Isotopic low-J CO lines[a]; this work
1.3×10^{23}	8	$N(^{13}CO) = 1.5 \times 10^{17}$ cm^{-2}, warm gas ($T_{kin} \geq 100$ K)[b]
7×10^{23}	11	$N(CS) = 2\text{–}18 \times 10^{14}$ cm^{-2}[c]
6.5×10^{23}	11	Continuum emission from FIR-peaks reanalyzed[c]
$\approx 3 \times 10^{22}$	15	$N(CS) \approx 3 \times 10^{13}$ cm^{-2}[d]
2.6×10^{23}	60	$N(H_2CO) = 7.9 \times 10^{13}$ cm^{-2}[e]
1.0×10^{23}	60	$N(CS) = 1.6 \times 10^{14}$ cm^{-2}[f]
8.6×10^{24}	11	1.3 mm continuum emission[g]

NOTE.—In most cases this is the sum of background and foreground, but foreground contribution can be neglected.

[a] Assumes $[^{13}CO]/[H_2] = 1.2 \times 10^{-6}$, $[C^{18}O]/[H_2] = 1.8 \times 10^{-7}$, $[C^{17}O]/[H_2] = 4.0 \times 10^{-8}$.

[b] Paper I, assumes $[^{13}CO]/[H_2] = 1.2 \times 10^{-6}$.

[c] Schulz et al. 1991; assumes $[CS]/[H_2] = 2.5 \times 10^{-9}$.

[d] Moore et al. 1989; assumes thermalized population of CS $J = 7 \rightarrow 6$ and $[CS]/[H_2] = 10^{-9}$.

[e] Mundy et al. 1987; assumes $[H_2CO]/[H_2] = 3 \times 10^{-10}$.

[f] Snell et al. 1984; assumes $[CS]/[H_2] = 1.6 \times 10^{-9}$.

[g] Mezger et al. 1988; calculated from their map (see text).

A detailed analysis of the ^{13}CO $J = 6 \rightarrow 5$ emission from these sources is under progress (Russell et al. 1993).

4.1.2. *Large Column Densities of Warm Gas*

In order to produce the strong ^{13}CO $J = 6 \rightarrow 5$ emission, the molecular hydrogen column density in the warm gas must be on the order of 10^{23} cm^{-2} or more. In the star formation regions we study here, this column density implies that between 10% and 50% of the gas mass is significantly heated by energetic processes associated with young stars. Such a high column density produces an optical depth of a few tenths in the ^{13}CO $J = 6 \rightarrow 5$ line, showing that the main isotope transition ^{12}CO $J = 6 \rightarrow 5$ is very optically thick in all observed sources. Our ^{13}CO $J = 6 \rightarrow 5$ measurements allow us to reliably find column densities in the warm gas well beyond those that could be estimated from the optically thick ^{12}CO lines alone.

We refine our estimates with an escape probability radiative transfer model (Stutzki & Winnewisser 1985). Lower limits for the molecular gas column density and temperature can be obtained if we assume that the gas density is high enough to keep the mid-J level populations close to local thermal equilibrium. Table 8 gives the temperatures and column densities required for $n_{H_2} = 10^6$ cm^{-3} to account for the emission in M17 and W51. In the case of S106 we used the intensity of the CO $14 \rightarrow 13$ line in order to further constrain the gas density. Assuming that the warm gas fills as much as 50% of the 64″ beam a minimum molecular hydrogen density of 3×10^5 cm^{-3} is required in order to explain the measured line intensities. The high column (and particle) densities somewhat lower the temperatures deduced for the warm gas component in earlier lower column density models. Therefore the gas temperatures we derive tend to be close to the lower end of the range allowed by earlier estimates based on comparisons of mid- and high-J ^{12}CO lines alone (Harris et al. 1987b).

TABLE 8

EXCITATION CONDITIONS DERIVED FROM MID-AND HIGH-J CO LINES

Source	T_{kin} (K)	n_{H_2} (cm^{-3})	N_{H_2} (cm^{-2})
M17	100	1×10^{6}[a]	1×10^{23}
W51 IRS 2	90	1×10^{6}[a]	1×10^{23}
S106[b]	90	3×10^{5}	1×10^{23}

NOTE.—Beam dilution effects are likely to increase the excitation parameters substantially.

[a] Assumed value.

[b] Assumes a beam-filling factor of 0.5 for the CO $14 \rightarrow 13$ line.

4.2. *What Heats the Molecular Gas?*

Almost all known star formation sites have detectable mid-J CO lines, indicating that warm dense gas is a very common phenomenon with, most likely, a common heating mechanism. Current theoretical models of photoheating in molecular clouds (PDR models: Tielens & Hollenbach 1985; Sternberg & Dalgarno 1989; Burton, Hollenbach, & Tielens 1990; van Dishoeck & Black 1988) successfully explain atomic fine-structure emission, but they cannot explain the observed high column densities of warm molecular gas. In spite of this, heating by UV photons is still the most attractive mechanism for producing significant column densities of warm *quiescent* molecular gas.

We have direct evidence that warm gas is located in the immediate vicinity of H II regions (M17, W51, Cepheus A), where the UV intensity is high. The spatial extent of the warm gas (≤ 1 pc) is usually larger than implied by its column-to-particle density ratio (typically $10^{23}/10^6$ cm = 0.03 pc). This indicates that the warm gas is clumpy, allowing a larger UV penetration (and heating) depth than in a homogeneous cloud (Stutzki et al. 1988; Boissé 1990; Howe et al. 1991). The UV heating interpretation is strongly supported by such spatial correlations and the fact that sources of lower UV intensity tend to emit weaker ^{13}CO $J = 6 \rightarrow 5$ lines.

The dust color temperatures of $T_{dust} \approx 50$ K (e.g., Chini et al. 1984) measured toward most dense cloud cores are substantially lower than the warm molecular gas temperatures, ruling out direct heating by collisions with warm dust. Enhanced gas temperatures are predicted by photodissociation region models, however, which allow gas temperatures up to an order of magnitude higher than the dust temperature close to the cloud edge (e.g., Tielens & Hollenbach 1985). The T^5 dependence of the far-IR emission from small dust particles makes the continuum cooling of the dust grains far too efficient to be balanced by the heat transfer from the gas to the dust. On the other hand, the cooling of the gas due to the collisions with the cooler dust is not much higher than the line cooling in the ^{13}CO lines (Paper I).

Stars that produce large amounts of radiation are likely to have substantial mechanical luminosity as well, raising the

possibility of shock excitation by fast winds. We can rule out shock heating for the bulk of the narrow-linewidth gas in the sources considered here (NGC 2024, S106, M17, W51, and Cepheus A), and for most sources we do not treat in detail (Table 3). Each individual source theoretically allows the possibility of excitation by shocks traveling perpendicular to the line of sight. However, it is extremely unlikely that all sources have the same preferred orientation of shock waves, independent of the source geometry. Shocks are likely to play an important role in the heating of the gas in higher velocity line wings in some sources (Orion, W51, W49; Jaffe et al. 1987).

Other possible mechanisms for heating quiescent gas are ambipolar diffusion or X-ray heating. An estimate of ambipolar diffusion heating efficiency in molecular clouds (Genzel 1991) indicates that ambipolar diffusion heating may contribute significantly to the heating of gas in the 50 K temperature range. X-ray heating may contribute in the vicinity of powerful OB associations (Genzel 1991), but it is very unlikely that either mechanism can heat column densities of 10^{23} cm^{-2} to temperatures ≥ 100 K.

Thus, the exclusion of a variety of heating mechanisms, combined with the spatial distribution of the warm gas, leads us to the conclusion that UV heating is very likely the dominant heating process in the warm quiescent gas. Discovery of an efficient shielding or formation process for CO molecules near the edges of photodissociation regions could eliminate the discrepancy between observed column densities and those predicted by current models.

4.3. *Gas and Dust in NGC 2024*

Armed with a knowledge of the amount, temperature, and placement of gas, we will be able to explore the connection between gas and dust in NGC 2024. One important question we can approach concerns the reliability of various tracers; for instance, do molecules in dense cold gas condense on dust grains to such an extent that molecular lines cannot arise from some regions? How unique are the results derived from different methods?

NGC 2024 is an example of a typical star formation region. The standard source model (Krügel et al. 1982; Crutcher et al. 1986) assumes that most of the molecular material in NGC 2024 lies in a dense ridge behind the optical H II region, which, in turn, is shadowed by a prominent dust lane. H_2CO and OH absorption lines are seen from the dust bar against the radio continuum (Crutcher et al. 1986; Barnes et al. 1989), while molecular emission lines arise from the material behind the H II region (e.g. Moore et al. 1989; Richer et al. 1989; Barnes & Crutcher 1990; Schulz et al. 1991). In the southern part of the source the background cloud and the foreground material seem to be connected and form the southern boundary of the H II region. This boundary is seen as an edge-on ionization front in the mid-IR (Grasdalen 1974) and in the radio continuum.

The continuum clumps FIR 1–6 (Mezger et al. 1988) are thought to be protostellar condensations embedded in the dense ridge. The similarity of the clumps in NGC 2024 suggests that they have formed at the same time, possibly induced by a compression wave from the expanding ionized bubble of the optical H II regon (e.g., Elmegreen & Lada 1977). Triggered star formation in NGC 2024 is also the likely explanation for the cluster of young stars found in NGC 2024 by Lada (1990) in her 2.2 μm survey.

4.3.1. *Line-of-Sight Structure*

In agreement with the velocity signature of centimeter wave absorption line measurements (Crutcher et al. 1986; Barnes et al. 1989), we assume that the emission centered on 9 km s^{-1} arises from material in front of the H II region, probably the same material producing the dark dust lane in the optical. No molecular absorption lines are seen at 11 km s^{-1}, indicating that the 11 km s^{-1} component is located behind the H II region.

The profiles of the ^{12}CO lines toward FIR 5 (Fig. 12) can then be explained by absorption of the 11 km s^{-1} background ^{12}CO emission in the 9 km s^{-1} foreground component. The optically thick ^{12}CO lines are likely to be intrinsically wider than the optically thin lines. Assuming intrinsic line width of ≈ 5 km s^{-1} centered on 11 km s^{-1}, the ^{12}CO transitions would suffer strong absorption by the colder 9 km s^{-1} foreground component. This absorption is seen directly in the CO $J = 3 \rightarrow 2$ line (Fig. 12). It extends from 8.5 to 12.5 km s^{-1}. This range is somewhat larger than suggested by the 9 km s^{-1} emission in the isotopic lines indicating that a fraction of the foregound material extends up to velocities around 12 km s^{-1}. At least part of the foreground gas is very cold (≤ 10 K) causing the deep absorption in ^{12}CO $3 \rightarrow 2$.

This foreground absorption in NGC 2024 could affect the CO $7 \rightarrow 6$ intensities. We are, however, confident that the map features are mostly due to variation of the emission component because the variations of the CO $7 \rightarrow 6$ center velocity are small and not correlated with the intensity of the 9 km s^{-1} feature. The low-velocity edge of the ^{12}CO line is apparently determined by a rather homogeneous foreground component which is optically thick up to LSR-velocities of $\approx$10–11 km s^{-1}.

Both source components are clearly seen in the double-peaked C^{18}O $2 \rightarrow 1$ line profiles around FIR 4 and FIR 5 (Fig. 14). North of the FIR 4 position the secondary peak in the C^{18}O spectra vanishes. The H_2CO absorption map by Crutcher et al. (1986) shows that the absorption in this region is weaker and shifts to higher velocities. Thus, the disappearance of the second emission component in C^{18}O is partly due to a decrease in column density, partly it is due to blending with the main component.

While the integrated intensity maps presented in § 3.2. do not allow us to distinguish between foreground and background emission, the C^{18}O channel maps (Fig. 15) reflect the morphology of NGC 2024 very well. North of FIR 6 the cloud splits into two parts bracketing the H II region. The part in front of the H II region dominates the emission at 8.5 and 9 km s^{-1}. It is still strong at 9.5 km s^{-1} but starts blending with the background component around FIR 3. Since the velocity gradients in the two components are opposite, there is a definite emission minimum at 10 km s^{-1} between FIR 5 and FIR 4, where the velocity difference is largest. At higher velocities the emission is fully dominated by the background, showing a clear velocity gradient (≈ -0.7 km s^{-1} arcmin^{-1}, corresponding to 5.8 km s^{-1} pc^{-1}, going north from FIR 5). An opposite velocity gradient is found in the foreground material ($\approx$0.4 km s^{-1} arcmin^{-1}, corresponding to 3.3 km s^{-1} pc^{-1}). These velocity gradients are consistent with a scenario where the expanding H II region pushes the molecular cloud apart.

South of FIR 6 we find emission in all velocity channels without a separation in two source components. This agrees with the standard source model, which assumes that the background and foreground components are connected and limit

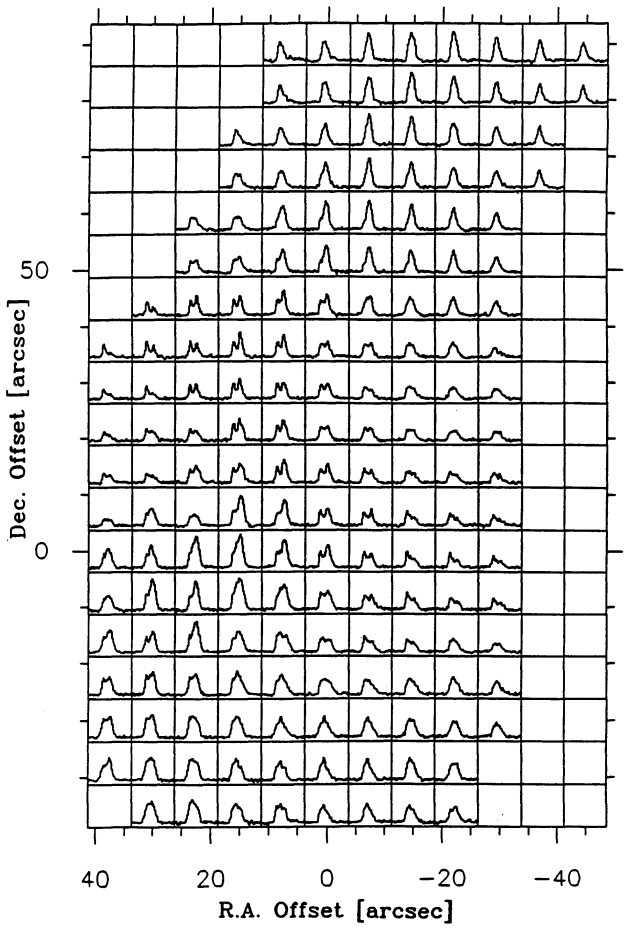

FIG. 14.—$C^{18}O$ $2 \rightarrow 1$ spectra measured toward NGC 2024. Offsets are relative to the FIR 5 position (Table 2). Note the secondary emission peak from the foreground material in the central part of the map.

the H II region toward the south, producing the sharp ionization front in the region of FIR 5.

Since the molecular line emission from NGC 2024 is dominated by the background component, which also contains the FIR peaks, the subsequent discussion will concentrate on that source component.

4.3.2. *Warm Gas in FIR 5?*

It is unlikely that the warm gas we find toward FIR 5 coexists with the cold (16 K) dust component proposed by Mezger et al. (1988). We find that the warm quiescent molecular gas in typical sources is found in the immediate vicinity of H II regions, which probably provide the bulk of the heating. Our ^{12}CO $7 \rightarrow 6$ and ^{13}CO $3 \rightarrow 2$ maps, which show features related to the H II region, indicate that this is certainly true for NGC 2024 (§ 3.2). Taking our column-to-particle density ratio estimate (≈ 0.03 pc) for the peak in NGC 2024 and accounting for clumpiness, this implies that most of the warm material seen in our CO maps probably lies within ≈ 0.1 pc of the H II region interface. At this distance from a $10^4\ L_\odot$ source the dust temperature should still be about 40 K, according to the dust temperature models by Scoville & Kwan (1976). This supports the dust model by Schulz et al. (1991), who fitted the far-IR and submm continuum with a ≈ 35 K dust component.

On the other hand, it is also unlikely that the warm gas and the putative cold dust are situated in different regions of space. The high-resolution maps of optically thin molecular line emission (Fig. 8) are very similar to the 1.3 mm continuum map by Mezger et al. (1988). Continuum maps and line maps show essentially the same morphological components of the source. This indicates at least a strong spatial correlation between the two emission regions.

Although we assume that radiation from the H II region supplies most of the heating to the gas, internal heating by hot embedded sources within the clumps may contribute to the large column density of warm gas. A number of indications for the presence of such embedded sources have been found (Richer 1990; Moore & Chandler 1989; Genzel & Downes 1977). Lis, Carstrom, & Phillips (1991) show that the dust emission can be explained both by externally or internally heated clumps.

Heating by embedded sources, while possibly important within the clumps, is not likely to contribute much to the bulk heating in NGC 2024, however. Assuming a luminosity of a few hundred $L_\odot$ for the object coincident with FIR 4, Moore & Chandler (1989) estimate a foreground visual extinction of ≤ 80 mag. The total CO column density we derive for FIR 5 corresponds to $A_v = 200$ mag, suggesting that the typical visual extinction in front of the FIR clumps is ≈ 100 mag. With $A_K/A_v = 0.112$ (Rieke & Lebofsky 1985) the typical K-band extinction is 2 mag higher than the upper limit Moore et al. found toward FIR 4. Thus, their nondetection of 2.2 μm sources in the other clumps indicates that possible embedded sources are not likely to be more luminous than a few 100 $L_\odot$. We should, however, emphasize the crudeness of this estimate, since the embedded objects could also be located toward the far side of the cloud and thus suffer higher extinction.

4.3.3. *Very Cold Gas in FIR 5?*

The optically thin low-J CO emission does not show a major contribution from cold molecular gas, although these transitions are most sensitive to high column densities of cold gas. The gas temperatures implied by the millimeter lines are almost as high as the temperatures derived from a high-temperature tracing line (^{13}CO $J = 6 \rightarrow 5$; Paper I). This is illustrated in Figure 16, which compares an escape probability radiative transfer model (Stutzki & Winnewisser 1985) with the measured line intensities. The model is calculated for the source parameters obtained from the LTE fit (§ 3.3, background component) and a molecular hydrogen density of 10^6 cm^{-3}. The data points are from the spectra observed toward FIR 5, integrated over the velocity range from 9.8 to 14 km s^{-1} in order to extract the contribution from the background component. All intensities have been scaled to the $C^{17}O$ abundance by multiplying by the abundance ratio and a factor $\tau/(1 - e^{-\tau})$ to correct for saturation.

Assuming molecular abundances similar to most molecular clouds, any low-temperature ($T < 25$ K) molecular gas in FIR 5 is restricted to column densities below 10^{23} cm^{-2} in order to be compatible with the observed line intensities. This is shown in Figure 16: the two low-temperature models both predict low-J CO line intensities about an order of magnitude higher than observed. If we allow a maximum contribution to the $C^{17}O$ $2 \rightarrow 1$ line temperature of 1 K from an additional cold (16 K) component, the $C^{17}O$ column density in this component is limited to $N(C^{17}O) \leq 10^{15}$ cm^{-2} (LTE case), which corresponds to $N_{H_2} \leq 3 \times 10^{22}$ cm^{-2}. This is about a factor of 300 lower than the column density derived by Mezger et al., based on the cold dust assumption.

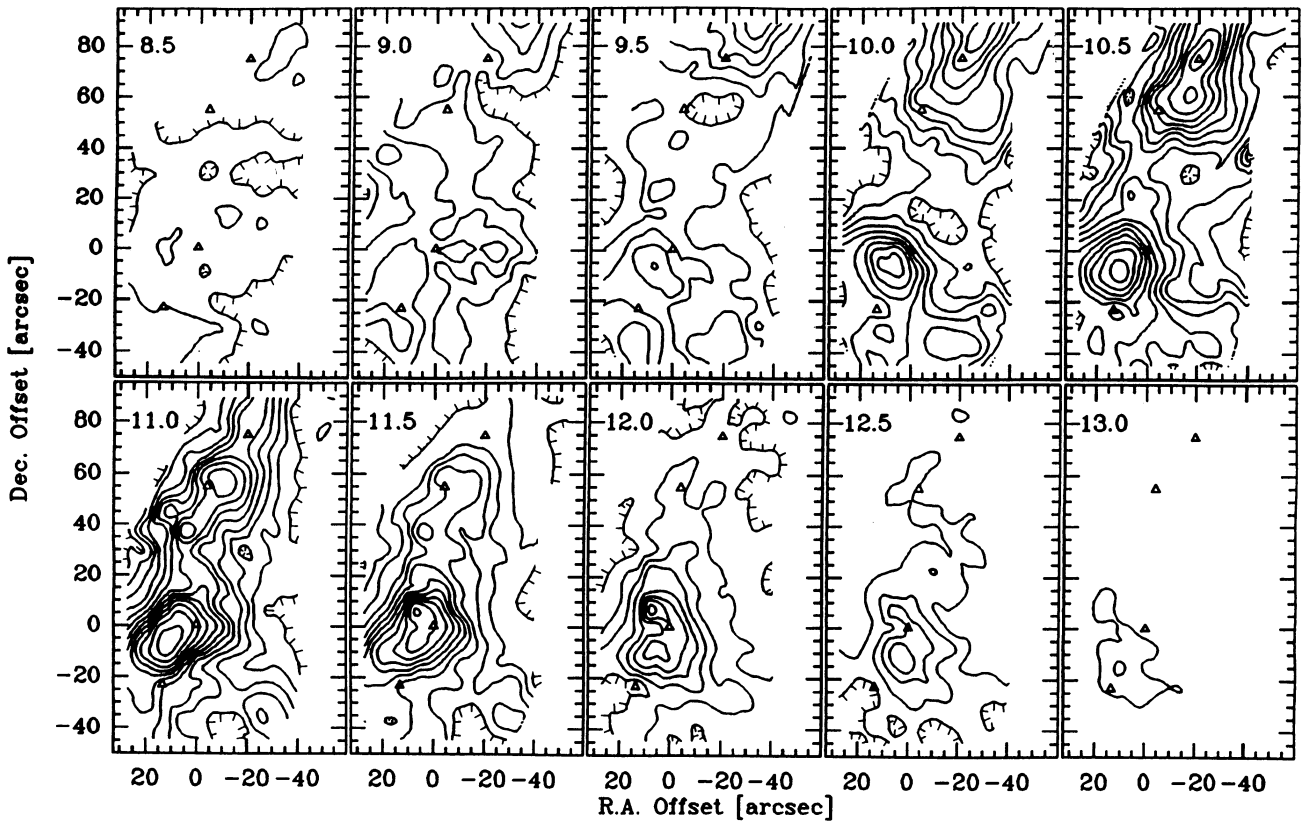

FIG. 15.—$C^{18}O$ $J = 2 \rightarrow 1$ channel maps of NGC 2024. The velocity channels are 0.5 km s^{-1} wide; center velocities are indicated on the individual panels. The contour levels are multiples of 1 K km s^{-1}.

It is of course possible that molecules condense onto the surfaces of very cold grains, as postulated by Mezger et al. (1988) and Mauersberger et al. (1992), radically changing the gas-to-dust ratio compared with warmer clouds. A depletion factor of approximately 100 would suppress the millimeter line fluxes sufficiently to resolve the column density discrepancy we find compared with the Mezger et al. (1988) results. If, however, the molecular lines traced only 1% of the total cloud material, we would expect larger discrepancies between the molecular line maps and the dust continuum map. As discussed in § 4.3.2, we consider it unlikely that the warm gas that dominates the molecular line maps could coexist with dust cold enough to freeze out 99% of the carbon monoxide.

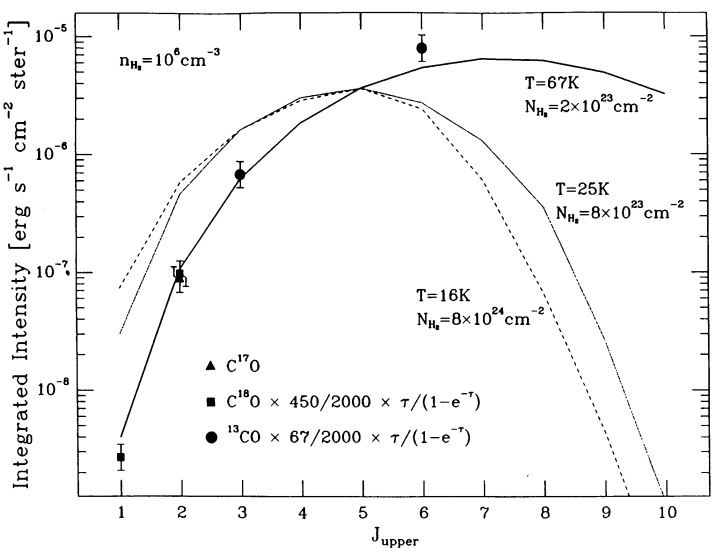

FIG. 16.—Radiative transfer model for the emission toward FIR 5. The solid line shows $C^{17}O$ line intensities calculated with an escape probability formalism. The source parameters are the ones obtained for the background component in the LTE fit (§ 3.3); the density is set to 10^6 cm^{-3}. The data points are from the measurements, scaled to the $C^{17}O$ abundance and corrected for saturation. For comparison we show two models at lower gas temperature (*dotted* and *dashed lines*).

A geometrical argument makes it unlikely we miss a substantial fraction of the column density in the clump cores. The column density we infer toward FIR 5 is consistent with the clump size seen in the low-J CO line maps (Fig. 8) and the density derived from CS measurements. Taking $n_{H_2} = 2 \times 10^6$ cm^{-3} (Schulz et al. 1991), our column density implies a linear thickness of the CO line-emitting region of 1×10^{17} cm. At the adopted distance of NGC 2024 (415 pc; Anthony-Twarog 1988), this corresponds to an angular distance of 16″. Assuming more or less spheroidal clumps, we would expect to find clump sizes of ≈20″ after convolving with a 13″ beam. In our $C^{17}O$ $J = 2 \rightarrow 1$ map, the largest clump has a FWHM of 23″ measured along a cut at $\Delta\delta = -10''$ (Fig. 8). Using a constant conversion factor from $C^{17}O$ $2 \rightarrow 1$ integrated intensity to column density (i.e. constant temperature and high enough density) the total mass contained in our $C^{17}O$ $2 \rightarrow 1$ map can be estimated to $\approx 40\ M_\odot$, most of which is concentrated in the region around FIR 5 and 6.

4.3.4. *A Temperature Gradient between Gas and Dust toward FIR 5?*

Since we know that we look through the H II region and warm gas to cooler material beyond, it is conceivable that the

cold dust is in the back part of the cloud, while the molecular lines arise only from a warmer foreground. The problem with this interpretation is that we would expect to find a transition region with gas temperatures high enough to prevent the bulk of the gas from freezing to grain surfaces. Independent of the exact temperature profile, the column density of gas between 20 and 30 K would have to be a few times 10^{23} cm^{-2} or higher. As we found above, this column would yield higher intensities in the low-J lines of the rare isotopes than we measured.

5. CONCLUSIONS

We have extended our ^{13}CO $J = 6 \rightarrow 5$ measurements to a large variety of star-forming regions. Sources spanning a luminosity range of six orders of magnitude have been observed in this transition. These observations confirm the existence of large amounts of warm, dense, quiescent molecular gas in most Galactic star-forming regions.

In regions of massive star formation, the typical physical conditions in this gas component are the following:

1. Mid-J lines of ^{12}CO are very optically thick.
2. The lower limit to the kinetic gas temperature is around 100 K. Due to the probable clumpiness of the sources, the temperatures are likely to be significantly higher.
3. Typical column densities in the warm gas component reach up to $N_{H_2} = 10^{23}$ cm^{-2} or higher.
4. The molecular hydrogen densities are high enough to keep the mid-J CO level population close to thermalized. This requires densities not substantially lower than 10^5 cm^{-3}.

The new measurements provide further evidence that the warm, dense, quiescent gas found in star formation regions is most likely to be heated by the energetic UV radiation escaping the H II regions ($\lambda > 912$ Å) around young stars. This is supported by the following arguments:

1. The warm gas shows narrow lines (typically $\Delta v \approx 5$ km s^{-1}), even in the very high excitation CO $J = 14 \rightarrow 13$ transition. The narrow-line widths are independent of the spatial orientation of the H II region/molecular cloud interface (M17, W51, large variety of sources). This makes shock heating very unlikely.
2. The warm quiescent gas is confined to a narrow zone (< 1 pc) close to the H II region (M17, W51, Cepheus A, NGC 2024) where the UV radiation is high.

Although present photodissociation region models do not predict the large amounts of warm gas observed in many sources, UV heating is still the most attractive process for producing substantial amounts of warm quiescent molecular gas near H II regions.

Our multiline study of NGC 2024 has shown that it is a typical case for a clumpy molecular cloud close to a luminous H II region. A large column density of molecular gas is heated by the UV radiation from the optical H II region, possibly with some additional internal heating provided by embedded young stellar cores.

In the special case of NGC 2024, this has implications for the millimeter continuum peaks (FIR 1–6) which have been interpreted as cold protostellar condensations. Our measurements show that the embedded FIR clumps are likely to be warm. This interpretation is based on the following arguments:

1. The counterparts of the continuum peaks are clearly seen in the maps of optically thin isotopic CO lines.
2. Our maps of different CO isotopes suggest that the clumps are located very close to the optical H II region.
3. The gas temperature toward FIR 5 derived from optically thin low-J transitions is around 70 K.
4. Our rare isotope CO observations exclude the presence of large amounts ($N_{H_2} \geq 10^{24}$ cm^{-2}) of cold ($T \leq 25$ K) molecular gas toward FIR 5.
5. It is unlikely that the temperature drops from ≥ 50 to ≤ 20 K without an extended layer at intermediate temperature which would otherwise appear in our low-J CO line observations.

Significant molecular depletion in regions of cold and dense gas cannot be rigorously excluded, but as the amount of information on the structure and heating sources increases, arguments requiring that a large fraction of the cloud could be at temperatures low enough to allow the depletion of molecules onto dust grains become less compelling.

We thank the staff of JCMT, UKIRT, IRAM 30 m, and KAO for their enthusiastic support during many observing runs. JCMT is operated by the Royal Observatory, Edinburgh, on behalf of the UK Science and Engineering Research Council, the Netherlands Organisation for Pure Research, and the National Research Council of Canada. We also thank J. Richer for contributing data prior to publication and S. Madden for help with the data reduction.

REFERENCES

Anthony-Twarog, B. J. 1982, AJ, 87, 1213
Baars, J. W. M., Güsten, R., Schulz, A., Steppe, H., & Thum, C. 1989, MPIfR Millimeter Tech. Div., Memorandum 71
Barnes, P. J., & Crutcher, R. M. 1990, ApJ, 351, 176
Barnes, P. J., Cruchter, R. M., Bieging, J. H., Storey, J. W. V., & Willner, S. P. 1939, ApJ, 342, 883
Boissé, P. 1990, A&A, 228, 483
Boreiko, R. T., & Betz, A. L. 1991, ApJ, 369, 382
Boreiko, R. T., Betz, A. L., & Zmuidzinas, J. 1989, ApJ, 337, 332
Burton, M. G., Hollenbach, D., & Tielens A. G. G. M. 1989, ApJ, 365, 620
Chandler, C. J., Gear, W. K. Sandell, G., Hayashi, S., Duncan, W. D., Griffin, M. J., & Hazell, A. S. 1990, MNRAS, 243, 330
Chini, R., Elsässer, H., & Neckel, Th. 1980, A&A, 91, 186
Chini, R., Kreysa, E., Mezger, P. G., & Gemünd, H.-P. 1984, A&A, 137, 117
Crutcher, R. M., Henkel, C., Wilson, T. L., Johnston, K. J., & Bieging, J. H. 1986, ApJ, 307, 302
Elmegreen, B. G., & Lada, C. J. 1977, ApJ, 214, 725
Genzel, R. 1991, in The Physics of Star Formation and Early Stellar Evolution, ed. C. J. Lada & N. D. Kylafis (Dordrecht: Kluwer), 155
Genzel, R., Becklin, E. E., Wynn-Williams, C. G., Moran, J. M., Reid, M. J., Jaffe, D. T., & Downes, D. 1982, ApJ, 255, 527
Genzel, R., & Downes, D. 1977, A&AS, 30, 145
Genzel, R., Poglitsch, A., & Stacey, G. J. 1988, ApJ, 333, L59
Graf, U. U. 1991, PhD. thesis, Ludwig-Maximilians-Universität, München
Graf, U. U., Genzel, R., Harris, A. I., Hills, R. E., Russell, A. P. G., & Stutzki, J. 1990, ApJ, 358, L49 (Paper I)
Grasdalen, D. L. 1974, ApJ, 193, 373
Harris, A. I. 1986, Ph.D. thesis, Univ. of California, Berkeley
Harris, A. I., Jaffe, D. T., Stutzki, J., & Genzel, R. 1987a, Int. J. Infrared Millimeter Waves, 8(8), 857
Harris, A. I., Stutzki, J., Genzel, R., Lugten, J. B., Stacey, G. J., & Jaffe, D. T. 1987b, ApJ, 322, L49
Harvey, P. M., Wilking, B. A., & Joy, M. 1984, ApJ, 278, 156
Henkel, C., Walmsley, C. M., & Wilson, T. L. 1980, A&A, 82, 41
Howe, J. E., Jaffe, D. T., Genzel, R., & Stacey, G. J. 1991, ApJ, 373, 158
Jaffe, D. T., Genzel, R., Harris, A. I., Lugten, J. B., Stacey, G. J., & Stutzki, J. 1989, ApJ, 344, 265
Jaffe, D. T., Harris, A. I., & Genzel, R. 1987, ApJ, 316, 231
Jiang, D. R., Perrier, C., & Léna, P. 1984, A&A, 135, 249
Krügel, E., et al. 1989, A&A, 211, 419
Krügel, E., Thum, C., Martín-Pintado, J., & Pankonin, V. 1982, A&AS, 48, 345
Lada, E. A. 1990, Ph.D. thesis, Univ. of Texas, Austin

Langer, W. D., & Penzias, A. A. 1990, ApJ, 357, 477
Lis, D. C., Carlstrom, J. E., & Phillips, T. G. 1991, ApJ, 370, 589
Martin, H. M., Sanders, D. B., & Hills, R. E. 1984, MNRAS, 208, 35
Mauersberger, R., Wilson, T. L., Mezger, P. G., Gaume, R., & Johnston, K. J. 1992, A&A, 256, 640
Mezger, P. G., Chini, R., Kreysa, E., Wink, J. E., & Salter, C. J. 1988, A&A, 191, 44
Moore, T. J. T., & Chandler, C. J. 1989, MNRAS, 241, 19P
Moore, T. J. T., Chandler, C. J., Gear, W. K., & Mountain, C. M. 1989, MNRAS, 237, 1P
Mundy, L. G., Evans, N. J., II, Snell, R. L., & Goldsmith, P. F. 1987, ApJ, 318, 392
Phillips, T. G., Knapp, R. G., Huggins, P. J., Werner, M. W., Wannier, P. G., Neugebauer, G., & Ennis, D. 1981, ApJ, 245, 512
Poglitsch, A., et al. 1991, Int. J. Infrared Millimeter Waves, 10(8), 859
Richer, J. S. 1990, MNRAS, 245, 24P
Richer, J. S., Hills, R. E., Padman, R., & Russell, A. P. G. 1989, MNRAS, 241, 231
Rieke, G. H., & Lebofsky, M. J. 1985, ApJ, 288, 618
Rodríguez, L. F., & Cantó, J. 1983, Rev. Mexicana Astron. Af., 8, 163
Russell, A. P. G., et al. 1993, in preparation
Schmid-Burgk, J., et al. 1989, A&A, 215, 150
Schulz, A., Güsten, R., Zylka, R., & Serabyn, E. 1991, A&A, 246, 570
Scoville, N. Z., & Kwan, J. 1976, ApJ, 206, 718
Snell, R. L., Mundy, L. G., Goldsmith, P. F., Evans, N. J., II, & Erikson, N. R. 1984, ApJ, 276, 625
Sternberg, A., & Dalgarno, A. 1989, ApJ, 338, 197
Stutzki, J., & Güsten, R. 1990, ApJ, 356, 513
Stutzki, J., Stacey, G. J., Genzel, R., Harris, A. I., Jaffe, D. T., & Lugten, J. B. 1988, ApJ, 332, 379
Stutzki, J., & Winnewisser, G. 1985, A&A, 148, 254
Thompson, R. I., Thronson, H. A., Jr., & Campbell, B. G. 1981, ApJ, 249, 622
Tielens, A. G. G. M., & Hollenbach, D. 1985, ApJ, 291, 722
van Dishoeck, E. F., & Black, J. H. 1988, ApJ, 334, 771
White, G. J., Phillips, J. P., Richardson, K. J., & Harten, R. H. 1986, A&A, 159, 309
Wilson, T. L., Fazio, G. G., Jaffe, D., Kleinmann, D., Wright, E. L., & Low, F. J. 1979, A&A, 76, 86